Angular analysis of the $e^+e^- \to D^{(*)\pm}D^{*\mp}$ process near the open charm threshold using initial-state radiation

V. Zhukova,[37,46] G. Pakhlova,[37,47] P. Pakhlov,[37,46] I. Adachi,[13,9] H. Aihara,[73] S. Al Said,[66,31] D. M. Asner,[58] V. Aulchenko,[3,56] T. Aushev,[47] R. Ayad,[66] V. Babu,[67] I. Badhrees,[66,30] P. Behera,[18] B. Bhuyan,[17] J. Biswal,[26] A. Bobrov,[3,56] G. Bonvicini,[77] A. Bozek,[53] M. Bračko,[42,26] T. E. Browder,[12] D. Červenkov,[4] V. Chekelian,[43] A. Chen,[50] B. G. Cheon,[11] K. Chilikin,[37,46] K. Cho,[32] S.-K. Choi,[10] Y. Choi,[65] D. Cinabro,[77] T. Czank,[71] N. Dash,[16] S. Di Carlo,[77] Z. Doležal,[4] Z. Drásal,[4] S. Eidelman,[3,56] H. Farhat,[77] J. E. Fast,[58] T. Ferber,[6] B. G. Fulsom,[58] V. Gaur,[76] A. Garmash,[3,56] R. Gillard,[77] P. Goldenzweig,[28] O. Grzymkowska,[53] E. Guido,[24] J. Haba,[13,9] K. Hayasaka,[55] H. Hayashii,[49] M. T. Hedges,[12] W.-S. Hou,[52] K. Inami,[48] G. Inguglia,[6] A. Ishikawa,[71] R. Itoh,[13,9] M. Iwasaki,[57] Y. Iwasaki,[13] W. W. Jacobs,[19] I. Jaegle,[7] H. B. Jeon,[35] S. Jia,[2] Y. Jin,[73] T. Julius,[44] K. H. Kang,[35] G. Karyan,[6] C. Kiesling,[43] D. Y. Kim,[64] K. T. Kim,[33] S. H. Kim,[11] S. Korpar,[42,26] D. Kotchetkov,[12] P. Križan,[38,26] P. Krokovny,[3,56] R. Kulasiri,[29] Y.-J. Kwon,[79] J. S. Lange,[8] L. Li,[61] L. Li Gioi,[43] D. Liventsev,[76,13] T. Luo,[59] M. Masuda,[72] T. Matsuda,[45] M. Merola,[23] K. Miyabayashi,[49] H. Miyata,[55] R. Mizuk,[37,46,47] G. B. Mohanty,[67] H. K. Moon,[33] T. Mori,[48] M. Nakao,[13,9] T. Nanut,[26] K. J. Nath,[17] M. Nayak,[77,13] M. Niiyama,[34] N. K. Nisar,[59] S. Nishida,[13,9] S. Ogawa,[70] S. L. Olsen,[62] H. Ono,[54,55] B. Pal,[5] C.-S. Park,[79] C. W. Park,[65] S. Paul,[69] I. Pavelkin,[47] T. K. Pedlar,[40] R. Pestotnik,[26] L. E. Piilonen,[76] V. Popov,[47] C. Pulvermacher,[13] A. Rostomyan,[6] Y. Sakai,[13,9] M. Salehi,[41,39] S. Sandilya,[5] T. Sanuki,[71] O. Schneider,[36] G. Schnell,[1,15] C. Schwanda,[21] Y. Seino,[55] K. Senyo,[78] M. E. Sevior,[44] V. Shebalin,[3,56] T.-A. Shibata,[74] J.-G. Shiu,[52] B. Shwartz,[3,56] F. Simon,[43,68] A. Sokolov,[22] E. Solovieva,[37,47] M. Starič,[26] T. Sumiyoshi,[75] M. Takizawa,[63,14,60] K. Tanida,[25] F. Tenchini,[44] K. Trabelsi,[13,9] M. Uchida,[74] S. Uehara,[13,9] T. Uglov,[37,47] Y. Unno,[11] S. Uno,[13,9] Y. Usov,[3,56] C. Van Hulse,[1] G. Varner,[12] A. Vinokurova,[3,56] V. Vorobyev,[3,56] E. Waheed,[44] C. H. Wang,[51] M.-Z. Wang,[52] P. Wang,[20] X. L. Wang,[58,13] Y. Watanabe,[27] S. Watanuki,[71] E. Won,[33] Y. Yamashita,[54] Y. Yusa,[55] S. Zakharov,[37] Z. P. Zhang,[61] V. Zhilich,[3,56] V. Zhulanov,[3,56] and A. Zupanc[38,26]

(Belle Collaboration)

[1]*University of the Basque Country UPV/EHU, 48080 Bilbao, Spain*
[2]*Beihang University, Beijing 100191, China*
[3]*Budker Institute of Nuclear Physics SB RAS, Novosibirsk 630090, Russia*
[4]*Faculty of Mathematics and Physics, Charles University, 121 16 Prague, Czech Republic*
[5]*University of Cincinnati, Cincinnati, Ohio 45221, USA*
[6]*Deutsches Elektronen–Synchrotron, 22607 Hamburg, USA*
[7]*University of Florida, Gainesville, Florida 32611, USA*
[8]*Justus-Liebig-Universität Gießen, 35392 Gießen, Germany*
[9]*SOKENDAI (The Graduate University for Advanced Studies), Hayama 240-0193, Japan*
[10]*Gyeongsang National University, Chinju 660-701, Korea*
[11]*Hanyang University, Seoul 133-791, Korea*
[12]*University of Hawaii, Honolulu, Hawaii 96822, USA*
[13]*High Energy Accelerator Research Organization (KEK), Tsukuba 305-0801, Japan*
[14]*J-PARC Branch, KEK Theory Center, High Energy Accelerator Research Organization (KEK), Tsukuba 305-0801, Japan*
[15]*IKERBASQUE, Basque Foundation for Science, 48013 Bilbao, Spain*
[16]*Indian Institute of Technology Bhubaneswar, Satya Nagar 751007, India*
[17]*Indian Institute of Technology Guwahati, Assam 781039, India*
[18]*Indian Institute of Technology Madras, Chennai 600036, India*
[19]*Indiana University, Bloomington, Indiana 47408, USA*
[20]*Institute of High Energy Physics, Chinese Academy of Sciences, Beijing 100049, China*
[21]*Institute of High Energy Physics, Vienna 1050, Austria*
[22]*Institute for High Energy Physics, Protvino 142281, Russia*
[23]*INFN—Sezione di Napoli, 80126 Napoli, Italy*
[24]*INFN—Sezione di Torino, 10125 Torino, Italy*
[25]*Advanced Science Research Center, Japan Atomic Energy Agency, Naka 319-1195, Japan*
[26]*J. Stefan Institute, 1000 Ljubljana, Slovenia*
[27]*Kanagawa University, Yokohama 221-8686, Japan*
[28]*Institut für Experimentelle Kernphysik, Karlsruher Institut für Technologie, 76131 Karlsruhe, Germany*
[29]*Kennesaw State University, Kennesaw, Georgia 30144, USA*

[30]*King Abdulaziz City for Science and Technology, Riyadh 11442, Saudi Arabia*
[31]*Department of Physics, Faculty of Science, King Abdulaziz University, Jeddah 21589, Saudi Arabia*
[32]*Korea Institute of Science and Technology Information, Daejeon 305-806, Korea*
[33]*Korea University, Seoul 136-713, Korea*
[34]*Kyoto University, Kyoto 606-8502, Japan*
[35]*Kyungpook National University, Daegu 702-701, Korea*
[36]*École Polytechnique Fédérale de Lausanne (EPFL), Lausanne 1015, Switzerland*
[37]*P.N. Lebedev Physical Institute of the Russian Academy of Sciences, Moscow 119991, Russia*
[38]*Faculty of Mathematics and Physics, University of Ljubljana, 1000 Ljubljana, Slovenia*
[39]*Ludwig Maximilians University, 80539 Munich, Germany*
[40]*Luther College, Decorah, Iowa 52101, USA*
[41]*University of Malaya, 50603 Kuala Lumpur, Malaysia*
[42]*University of Maribor, 2000 Maribor, Slovenia*
[43]*Max-Planck-Institut für Physik, 80805 München, Germany*
[44]*School of Physics, University of Melbourne, Victoria 3010, Australia*
[45]*University of Miyazaki, Miyazaki 889-2192, Japan*
[46]*Moscow Physical Engineering Institute, Moscow 115409, Russia*
[47]*Moscow Institute of Physics and Technology, Moscow Region 141700, Russia*
[48]*Graduate School of Science, Nagoya University, Nagoya 464-8602, Japan*
[49]*Nara Women's University, Nara 630-8506, Japan*
[50]*National Central University, Chung-li 32054, China*
[51]*National United University, Miao Li 36003, China*
[52]*Department of Physics, National Taiwan University, Taipei 10617, Taiwan*
[53]*H. Niewodniczanski Institute of Nuclear Physics, Krakow 31-342, Poland*
[54]*Nippon Dental University, Niigata 951-8580, Japan*
[55]*Niigata University, Niigata 950-2181, Japan*
[56]*Novosibirsk State University, Novosibirsk 630090, Russia*
[57]*Osaka City University, Osaka 558-8585, Japan*
[58]*Pacific Northwest National Laboratory, Richland, Washington 99352, USA*
[59]*University of Pittsburgh, Pittsburgh, Pennsylvania 15260, USA*
[60]*Theoretical Research Division, Nishina Center, RIKEN, Saitama 351-0198, Japan*
[61]*University of Science and Technology of China, Hefei 230026, China*
[62]*Seoul National University, Seoul 151-742, Korea*
[63]*Showa Pharmaceutical University, Tokyo 194-8543, Japan*
[64]*Soongsil University, Seoul 156-743, Korea*
[65]*Sungkyunkwan University, Suwon 440-746, Korea*
[66]*Department of Physics, Faculty of Science, University of Tabuk, Tabuk 71451, Saudi Arabia*
[67]*Tata Institute of Fundamental Research, Mumbai 400005, India*
[68]*Excellence Cluster Universe, Technische Universität München, 85748 Garching, Germany*
[69]*Department of Physics, Technische Universität München, 85748 Garching, Germany*
[70]*Toho University, Funabashi 274-8510, Japan*
[71]*Department of Physics, Tohoku University, Sendai 980-8578, Japan*
[72]*Earthquake Research Institute, University of Tokyo, Tokyo 113-0032, Japan*
[73]*Department of Physics, University of Tokyo, Tokyo 113-0033, Japan*
[74]*Tokyo Institute of Technology, Tokyo 152-8550, Japan*
[75]*Tokyo Metropolitan University, Tokyo 192-0397, Japan*
[76]*Virginia Polytechnic Institute and State University, Blacksburg, Virginia 24061, USA*
[77]*Wayne State University, Detroit, Michigan 48202, USA*
[78]*Yamagata University, Yamagata 990-8560, Japan*
[79]*Yonsei University, Seoul 120-749, Korea*

(Received 28 July 2017; published 10 January 2018)

We report a new measurement of the exclusive $e^+e^- \to D^{(*)\pm}D^{*\mp}$ cross sections as a function of the center-of-mass energy from the $D^{(*)\pm}D^{*\mp}$ threshold through $\sqrt{s} = 6.0$ GeV, using the initial-state

radiation technique. The analysis is based on a data sample collected with the Belle detector with an integrated luminosity of 951 fb^{-1}. The accuracy of the cross section measurement is increased by a factor of 2 over the first Belle study. We perform the first angular analysis of the $e^+e^- \to D^{*\pm}D^{*\mp}$ process and decompose this exclusive cross section into three components corresponding to the D^* helicities.

DOI: 10.1103/PhysRevD.97.012002

I. INTRODUCTION

Parameters, like masses, widths, and electronic widths, of the vector charmonia (ψ's) lying above the open-charm threshold were obtained from the total e^+e^- cross section to hadronic final states in measurements by MARK-I, DELCO, DASP, MARK-II, Crystal Ball, and BES [1]. In 2008, BES reanalyzed their data taking into account the interference between ψ states and the relative phases of their amplitudes but using model predictions for the ψ decays to two-body open-charm final states [2]. As a result, the obtained parameters of the ψ states cannot be regarded as universal and model independent. Notably, BES did not extract the parameters of other vector charmoniumlike resonances, such as Y(4008), Y(4260), Y(4360) and Y(4660), which were observed by *BABAR* [3–5] and Belle [6–10] in e^+e^- annihilation. Y(4008) and Y(4260) decay into the $J/\psi\pi^+\pi^-$ final state while Y(4360) and Y(4660) decay into $\psi(2S)\pi^+\pi^-$. The Y states do not appear as peaks either in the total hadronic cross section or in the exclusive e^+e^- cross sections to open-charm final states that were measured later. In addition, there exist predictions in the literature that some of the Y states could manifest themselves as coupled-channel effects [11].

A detailed study of the exclusive e^+e^- cross sections to open-charm final states could help establish parameters of the vector charmonia and charmoniumlike states in a model-independent way and, therefore, to shed light on the nature of the Y family. Such exclusive e^+e^- cross sections to various open-charm final states were first measured at B-factories by Belle [12–17] and *BABAR* [18–20] using the initial-state radiation (ISR) processes, and by CLEO [21] using an energy scan in the range $\sqrt{s} = 3.97$–4.26 GeV. The ISR process, in which a hard photon with a significant part of the initial energy is emitted before the electron-positron annihilation, allows one to measure e^+e^- cross sections at the center-of-mass energies below the energy of the B-factory. Belle has demonstrated that, in the studied energy region, the total hadronic cross section is almost saturated by the sum of the two-body ($D^{(*)}\bar{D}^{(*)}$, $D_s^{(*)+}D_s^{(*)-}$, $\Lambda_c^+\Lambda_c^-$) and three-body $D\bar{D}^{(*)}\pi$ cross sections, after the subtraction of the u-, d-, and s-continuum [22]. The main contribution to the inclusive open-charm cross section comes from the $D\bar{D}$, $D\bar{D}^*$, and $D^*\bar{D}^*$ final states.

The first attempt to extract the parameters of the ψ states (in particular, their couplings to the open-charm channels) from a combined coupled-channel fit for all exclusive open-charm cross sections was performed in Ref. [23]. At the time, although the suggested approach provides a good overall description of the line shapes, reliable conclusions could not be made because of the limited statistical accuracy of the data and because of the absence of experimental information on each of the three helicity amplitudes of the $D^*\bar{D}^*$ system. For further details, see Ref. [23] and references therein.

Here, we report a new measurement of the exclusive $e^+e^- \to D^{(*)+}D^{*-}$ cross sections as a function of the center-of-mass energy near the $D^{(*)+}D^{*-}$ threshold in the initial-state radiation processes.[1] Compared to Ref. [13], the larger data set, the improved track reconstruction, and the additional modes used in the D and D^* reconstruction allow one to obtain more precise determination of these cross sections. We also perform the first angular analysis of the $e^+e^- \to D^{*\pm}D^{*\mp}$ processes and explicitly decompose these exclusive cross sections into the three components corresponding to the D^*'s helicities. Employing a coupled-channel technique—following the lines of Ref. [23], for example—a future study could use these results to extract the parameters of the vector charmonium states.

II. DATA SAMPLE AND BELLE DETECTOR

The analysis reported in this work is based on the data sample with an integrated luminosity of 951 fb^{-1} collected with the Belle detector [24] at the KEKB asymmetric-energy e^+e^- collider near the energies of the $\Upsilon(4S)$ and $\Upsilon(5S)$ resonances [25].

The Belle detector is a large-solid-angle magnetic spectrometer that consists of a silicon vertex detector, a 50-layer central drift chamber (CDC), an array of aerogel threshold Cherenkov counters (ACC), a barrel-like arrangement of time-of-flight scintillation counters (TOF), and an electromagnetic calorimeter (ECL) composed of CsI(Tl) crystals located inside a superconducting solenoid coil that provides a 1.5 T magnetic field. An iron flux return located outside of the coil is instrumented to detect K_L^0 mesons and to identify muons (KLM). A detailed description of the detector can be found, for example, in Ref. [24].

III. METHOD

To select the $e^+e^- \to D^{(*)+}D^{*-}\gamma_{\rm ISR}$ signal, we use the method described in Ref. [13]. We require full reconstruction of only one of the D^{*+} (for

[1]Charge-conjugate modes are included throughout this paper.

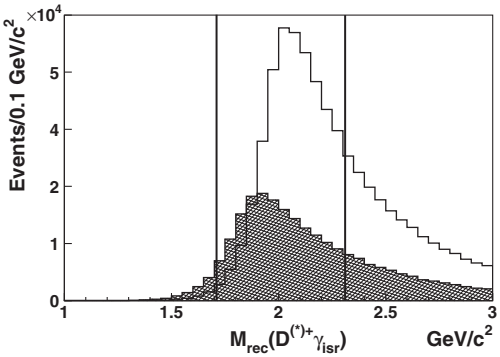

FIG. 1. MC simulation $M_{\rm rec}(D^{(*)+}\gamma_{\rm ISR})$ spectra for $e^+e^- \to D^{*+}D^{*-}\gamma_{\rm ISR}$ (histogram) and $e^+e^- \to D^+D^{*-}\gamma_{\rm ISR}$ (hatched histogram). The signal window is shown by vertical lines.

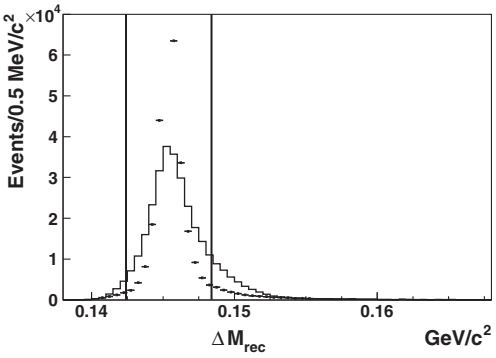

FIG. 2. The $\Delta M_{\rm rec}$ distributions before (histogram) and after (points with errors) the refit procedure for the MC events of $e^+e^- \to D^{*+}D^{*-}\gamma_{\rm ISR}$. The signal window lies between vertical lines.

$e^+e^- \to D^{*+}D^{*-}$) or D^+ mesons (for $e^+e^- \to D^+D^{*-}$), the $\gamma_{\rm ISR}$ photon, and the slow pion from the other D^{*-}. The partial D^{*-} reconstruction without reconstruction of the $\bar{D}^0$ daughter of the D^{*-} increases the overall efficiency by a factor of $\sim$20 for $e^+e^- \to D^{*+}D^{*-}$ and $\sim$10 for $e^+e^- \to D^+D^{*-}$, while suppressing the backgrounds enough to be able subtract them reliably using the data. Unlike the usual method for reconstruction of ISR processes, where the hadronic final state is fully reconstructed and $\gamma_{\rm ISR}$ is inferred from the spectrum of masses recoiling against the hadronic system, we require here that the $\gamma_{\rm ISR}$ be reconstructed. This requirement does not significantly decrease the efficiency as the slow pion from $D^{*\pm}$ decay has a low reconstruction efficiency when $\gamma_{\rm ISR}$ is outside the detector acceptance (because of the very low transverse momentum of $\gamma_{\rm ISR}$ in this case).

The recoil mass against the X system is defined as[2]

$$M_{\rm rec}(X) = \sqrt{(E_{\rm cm} - E_X)^2 - p_X^2}, \quad (1)$$

where $E_{\rm cm}$ is the e^+e^- center-of-mass energy, and E_X and p_X are the center-of-mass energy and momentum of the X system, respectively.

For the signal candidates, the spectrum of mass recoiling against the $D^{(*)+}\gamma_{\rm ISR}$ system peaks at the D^{*-} mass. According to a Monte Carlo (MC) study, this peak is wide ($\sigma \sim 150$ MeV/c^2) and asymmetric due to the asymmetric photon energy resolution function and higher-order ISR corrections (i.e., more than one $\gamma_{\rm ISR}$ in the event). Because of poor $M_{\rm rec}(D^{(*)+}\gamma_{\rm ISR})$ resolution, the signals from $D\bar{D}$, $D\bar{D}^*$, and $D^*\bar{D}^*$ overlap strongly; hence, one cannot distinguish these processes using this measurement alone. For illustration, Fig. 1 shows the MC $M_{\rm rec}(D^{*+}\gamma_{\rm ISR})$ spectra for the $e^+e^- \to D^{*+}D^{*-}\gamma_{\rm ISR}$ and $e^+e^- \to D^+D^{*-}\gamma_{\rm ISR}$ processes.

To resolve this, we use the information provided by the slow pion from the unreconstructed D^{*-} meson. The distribution of the difference between the masses recoiling against the $D^{(*)+}\gamma_{\rm ISR}$ and $D^{(*)+}\pi^-_{\rm slow}\gamma_{\rm ISR}$, termed the recoil-mass difference,

$$\Delta M_{\rm rec} = M_{\rm rec}(D^{(*)+}\gamma_{\rm ISR}) - M_{\rm rec}(D^{(*)+}\pi^-_{\rm slow}\gamma_{\rm ISR}), \quad (2)$$

has a narrow peak for the signal process around the $m_{D^{*+}} - m_{D^0}$ mass difference (Fig. 2, histogram). The resolution of this peak is below 2 MeV/c^2 as the uncertainty of the $\gamma_{\rm ISR}$ momentum is mostly canceled out for this variable. Thus, the existence of a partially reconstructed D^{*-} in the event is identified by the presence of this peak. The method does not exclude contributions in the $\Delta M_{\rm rec}$ signal window from processes with extra neutrals in the final state (e.g., $e^+e^- \to D^{(*)+}D^{*-}\pi^0$). However, this background is suppressed and its residual contribution can be reliably determined using the data, as discussed in the data analysis section.

To measure the exclusive cross sections as a function of $\sqrt{s}$, one needs to obtain the $D^{(*)+}D^{*-}$ mass spectrum despite one of D^* mesons being unreconstructed. In the absence of higher-order QED processes, the $D^{(*)+}D^{*-}$ mass corresponds to the mass recoiling against the single ISR photon: $M(D^{(*)+}D^{*-}) \equiv M_{\rm rec}(\gamma_{\rm ISR})$. However, the poor $M_{\rm rec}(\gamma_{\rm ISR})$ resolution ($\sigma \sim 120$ MeV/c^2) because of a large uncertainty in the measurement of the photon momentum precludes the study of relatively narrow charmonium states in the $D^{(*)+}D^{*-}$ mass spectra. To improve the $M_{\rm rec}(\gamma_{\rm ISR})$ resolution, we refit the recoil mass against the $D^{(*)+}\gamma_{\rm ISR}$ system, constrained to the D^{*-} mass. This procedure utilizes the well-measured momentum of the

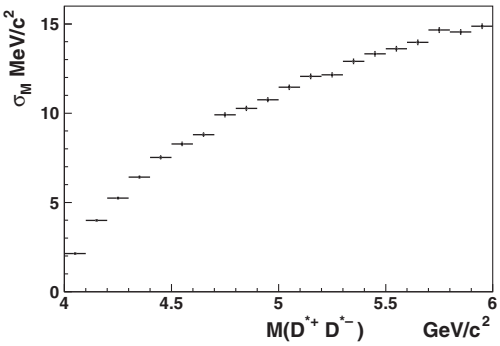

FIG. 3. The $D^{*+}D^{*-}$ mass resolution after the refit procedure as a function of $M(D^{*+}D^{*-})$ for the process $e^+e^- \to D^{*+}D^{*-}\gamma_{\rm ISR}$.

[2]Here, the speed of light is set to unity for convenience.

reconstructed $D^{(*)+}$ meson and the signal kinematics to better determine the momentum of the ISR photon. It works well even in the case of a second ISR photon, as checked with the MC. As a result, the $M_{\rm rec}(\gamma_{\rm ISR})$ resolution is drastically improved: near the threshold, the resolution is better than 3 MeV/c^2, and smoothly increases to 15 MeV/c^2 at $\sqrt{s} \sim$ 6 GeV (Fig. 3). The resolution of the recoil-mass difference after refit, $\Delta M_{\rm rec}^{\rm fit}$, improves by a factor of ∼2 (Fig. 2, points with error bars); this is exploited for more effective suppression of the combinatorial background.

IV. MONTE CARLO STUDY AND CALIBRATION OF $\gamma_{\rm ISR}$ ENERGY

The simulation of the signal and background processes up to the second-order ISR corrections and vacuum-polarization corrections is performed using the PHOKHARA MC generator [26]. In the signal-MC samples, the $D^{(*)+}D^{*-}$ characteristics (mass spectrum and angular distributions) are tuned to those measured in the data. As the measured distributions are extracted from the data using the MC simulation, this tuning is repeated until the difference between successive iterations is negligibly small.

To improve the accuracy of the MC simulation, we calibrate the photon energy. For soft and medium energy photons, this is done using $\pi^0 \to \gamma\gamma$ [27]. For energetic (∼4 GeV) photons, where there are few energetic π^0 in the data, we select a clean sample of fully reconstructed $e^+e^- \to \psi(2S)\gamma_{\rm ISR} \to J/\psi\pi^+\pi^-\gamma_{\rm ISR}$ events and study the spectrum of the mass recoiling against $\gamma_{\rm ISR}$; a broad peak around the $\psi(2S)$ mass is expected. A small shift between MC and data is observed, from which a correction factor for the photon energy is determined to be 0.9980 ± 0.0004. We apply this correction throughout the analysis.

V. DATA SAMPLE AND EVENT SELECTION

In the first Belle analysis [13], the strategy was to select a clean sample of the studied process with minimal background contribution to provide the most reliable result. It was demonstrated there that all backgrounds were well under control and were subtracted reliably using the data. The aim of the present analysis is to improve the accuracy of the cross section measurement. Therefore, we reoptimize the selection criteria and add more $D^{(*)}$ decay modes.

All charged tracks are required to be consistent with origination from the interaction point (IP): we require $dr <$ 2 cm and $|dz| < 4$ cm, where dr and $|dz|$ are the impact parameters perpendicular to and along the beam direction, respectively, with respect to the IP. Information from the TOF, the number of the photoelectrons from the ACC and the dE/dx measurement in the CDC are combined to form a likelihood $\mathcal{L}$ for hadron identification. Charged kaon candidates are required to have a kaon/pion likelihood ratio $\mathcal{P}_{K/\pi} = \mathcal{L}_K/(\mathcal{L}_K + \mathcal{L}_\pi) > 0.6$. The identification efficiencies typically exceed 90%, while misidentification probabilities are less than 10% [28]. No identification requirements are applied for pion candidates, as the pion multiplicity is much higher than that of other hadrons. K_S^0 candidates are reconstructed by combining $\pi^+\pi^-$ pairs with an invariant mass within ± 15 MeV/c^2 ($\approx \pm 5\sigma$) of the K_S^0 mass. The distance between the two pion tracks at the K_S^0 vertex must be less than 1 cm. The transverse flight distance from the interaction point is required to be greater than 0.1 cm, and the angle between the K_S^0 momentum direction and the line joining the decay vertex and the IP in the transverse plane should be smaller than 0.1 rad. Photons are reconstructed in the electromagnetic calorimeter as showers with energy greater than 50 MeV that are not associated with charged tracks. ISR photon candidates are required to have a center-of-mass energy above 3.0 GeV. Combinations of two photons are treated as a π^0 candidates if their invariant mass lies within 15 MeV/c^2 ($\approx \pm 3\sigma$) of the nominal π^0 mass. Such combinations are then refitted with a π^0 mass constraint to improve the π^0 momentum resolution.

D^0 candidates are reconstructed in nine decay modes: $K^-\pi^+$, K^-K^+, $K^-\pi^-\pi^+\pi^+$, $K_S^0\pi^+\pi^-$, $K^-\pi^+\pi^0$, $K_S^0K^+K^-$, $K_S^0\pi^0$, $K^-K^+\pi^-\pi^+$, and $K_S^0\pi^+\pi^-\pi^0$. D^+ candidates are reconstructed using the $K^+\pi^+\pi^-$, $K_S^0\pi^+$, and $K_S^0K^+$ channels. The mass window for all modes without (with) π^0 is ± 15 MeV/c^2 (± 20 MeV/c^2) of the nominal D^0 or D^+ mass [1], corresponding to $\approx \pm 3\sigma$ in each case. A mass-constrained vertex fit is applied to the D^0 and D^+ candidates to improve their momentum resolution.

D^{*+} candidates are selected in the $D^0\pi^+$ decay mode; the D^{*0} candidates are selected in the $D^0\pi^0$ mode and are used for background studies. In both cases, the signal window for the D^* mass is chosen to be ± 3 MeV/c^2 ($\approx 3\sigma$) of the nominal D^{*0} or D^{*+} mass [1].

To increase the efficiency, the $M_{\rm rec}(D^{(*)+}\gamma_{\rm ISR})$ signal region is defined to be ± 300 MeV/c^2 of the D^{*-} meson mass (see Fig. 1). The process $e^+e^- \to D^{(*)+}D^{*-}\pi^0_{\rm miss}\gamma_{\rm ISR}$ has the $M_{\rm rec}(D^{(*)+}\gamma_{\rm ISR})$ spectrum shifted to higher values, but still overlaps this signal window. We eschewed a further extension of the signal window to the higher masses since this would lead to an increased contribution from the background process with an extra π^0. The $\Delta M_{\rm rec}^{\rm fit}$ value is required to be within ± 3 MeV/c^2 of the $m_{D^{*+}} - m_{D^0}$ value (see Fig. 2).

The fraction of events with more than one candidate passing all selection criteria is small (3%). For these, we select the one with the smallest value of

$$\chi^2 = \chi^2_{M(D)}(+\chi^2_{M(D^*)}) + \chi^2_{\Delta M_{\rm rec}^{\rm fit}}, \tag{3}$$

where χ_i^2 is defined as a squared ratio of the difference between the measured and expected observable i to the corresponding resolution. For the background studies, we use $M(D^{(*)+})$ and $\Delta M_{\rm rec}^{\rm fit}(D^{(*)+}\gamma_{\rm ISR})$ sidebands. In the sideband regions, a similar selection of a single candidate per event is performed based on a χ^2 calculated with respect to the center of the corresponding sideband interval.

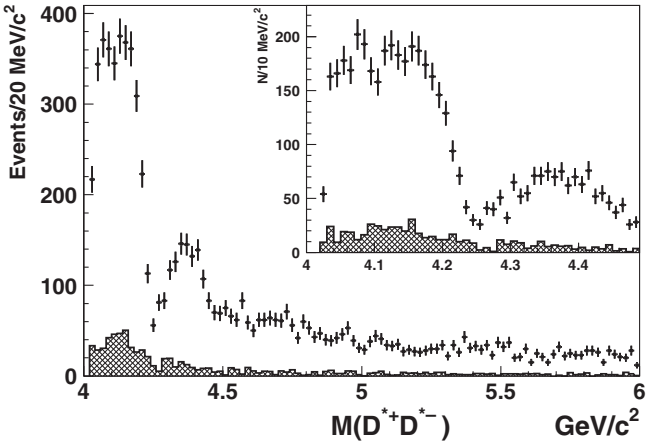

FIG. 4. The $M(D^{*+}D^{*-})$ spectrum in the data after applying all selection criteria (points with error bars). The sum of backgrounds (1)–(3) is shown as the hatched histogram. The inset shows the zoomed spectrum near the threshold with a finer (half-size) bin width of 10 MeV/c^2.

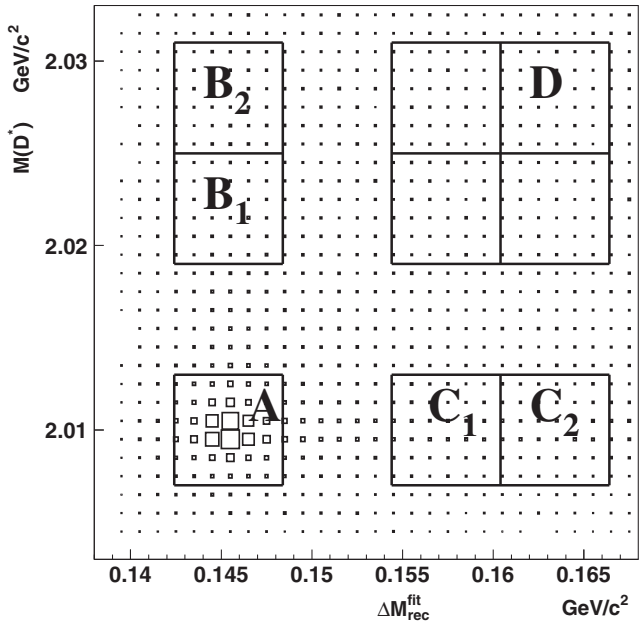

FIG. 5. The scatter plot of $M(D^{*+})$ vs $\Delta M_{\rm rec}^{\rm fit}$ in the data.

VI. DATA ANALYSIS

As the process $e^+e^- \to D^{*+}D^{*-}\gamma_{\rm ISR}$ contributes to the $e^+e^- \to D^+D^{*-}\gamma_{\rm ISR}$ when one of the $D^{*\pm}$ mesons decays into $D^+\pi^0$ or $D^+\gamma$, we study the process $e^+e^- \to D^{*+}D^{*-}$ first. Then we use the obtained result to correct the $e^+e^- \to D^{*+}D^{*-}\gamma_{\rm ISR}$ Monte Carlo and use the latter to extract the information that is needed to subtract the $D^{*+}D^{*-}$ contribution from the $e^+e^- \to D^+D^{*-}\gamma_{\rm ISR}$ process.

A. Measurement of $e^+e^- \to D^{*+}D^{*-}\gamma_{\rm ISR}$

The $D^{*+}D^{*-}$ mass spectrum, after applying all the selection criteria, is shown in Fig. 4. Taking advantage of the fine $M(D^{*+}D^{*-})$ resolution at the threshold and higher statistics in comparison with the first Belle paper [13], we study the mass structure near the threshold with finer bins. The $D^{*+}D^{*-}$ mass spectrum is presented in the inset of Fig. 4.

We consider the following background contributions:

(1) combinatorial background under the reconstructed D^{*+} peak, when the slow pion is truly a D^{*-} daughter;
(2) real D^{*+} mesons combined with a combinatorial (random) slow pion;
(3) both the D^{*+} meson and slow pion are combinatorial;
(4) reflections from the processes $e^+e^- \to D^{*+}D^{*-}\pi^0\gamma_{\rm ISR}$ where the π^0 is lost;
(5) $e^+e^- \to D^{*+}D^{*-}\pi^0_{\rm fast}$ where the hard $\pi^0_{\rm fast}$ is misidentified as $\gamma_{\rm ISR}$. This can happen if the two photons from the $\pi^0_{\rm fast}$ decay merge into one ECL cluster or, in the case of an asymmetric $\pi^0_{\rm fast}$ decay, if one of the photons carries a large fraction of the $\pi^0_{\rm fast}$ energy.

The contribution from the combinatorial backgrounds, i.e., the first three background sources, is extracted using the $M(D^{*+})$ and $\Delta M_{\rm rec}^{\rm fit}$ sidebands. The $M(D^{*+})$ vs $\Delta M_{\rm rec}^{\rm fit}$ scatter plot is shown in Fig. 5 for the data. The signal region (indicated as box **A**) is defined by the requirement that $M(D^{*+})$ and $\Delta M_{\rm rec}^{\rm fit}$ lie within ± 3 MeV/c^2 of the corresponding nominal values. The contributions of combinatorial D^{*+} candidates or random slow pions—backgrounds (1) and (2)—are estimated from the regions shown by boxes **B** and **C**, respectively. The sidebands of double the width are shifted from the signal region to avoid signal oversubtraction. Background (3) is present in both $M(D^{*+})$ and $\Delta M_{\rm rec}^{\rm fit}$ sidebands and therefore is subtracted twice. To correct for this oversubtraction, the double sideband region **D** is used.

The total contribution to the $M(D^{*+}D^{*-})$ spectrum from the combinatorial backgrounds (1)–(3) is calculated according to the formula

$$M_{\rm bg\,(1)\text{-}(3)} = 0.58 \cdot M_{\mathbf{B}} + 0.53 \cdot M_{\mathbf{C}} - 0.307 \cdot M_{\mathbf{D}}, \quad (4)$$

where $M_{\mathbf{B,C,D}}$ are the $D^{*+}D^{*-}$ mass spectra from the **B**, **C**, and **D** sidebands, respectively, and the scaling factors are calculated to provide normalization of the corresponding background contributions within the signal window. To obtain these scaling factors, the distributions of $M(D^{*+})$ and $\Delta M_{\rm rec}^{\rm fit}$ are fit using signal shapes fixed to those from the MC simulation and the following background parametrization:

$$f_{\rm bg} = a\sqrt{x - x_{\rm thr}} \cdot (1 + bx + cx^2), \quad (5)$$

where x is the $M(D^{*+})$ or $\Delta M_{\rm rec}^{\rm fit}$, $x_{\rm thr}$ is a corresponding threshold value, and a, b, and c are free parameters. The fit results are shown in Fig. 6.

The total combinatorial background (1)–(3), calculated according to Eq. (4), is shown in Fig. 4 as the hatched histogram.

To estimate the contribution from background (4), the process $e^+e^- \to D^{*+}D^{*-}\pi^0_{\rm miss}\gamma_{\rm ISR}$, we study the isospin-conjugated process $e^+e^- \to D^{*0}D^{*-}\pi^+_{\rm miss}\gamma_{\rm ISR}$ using a similar

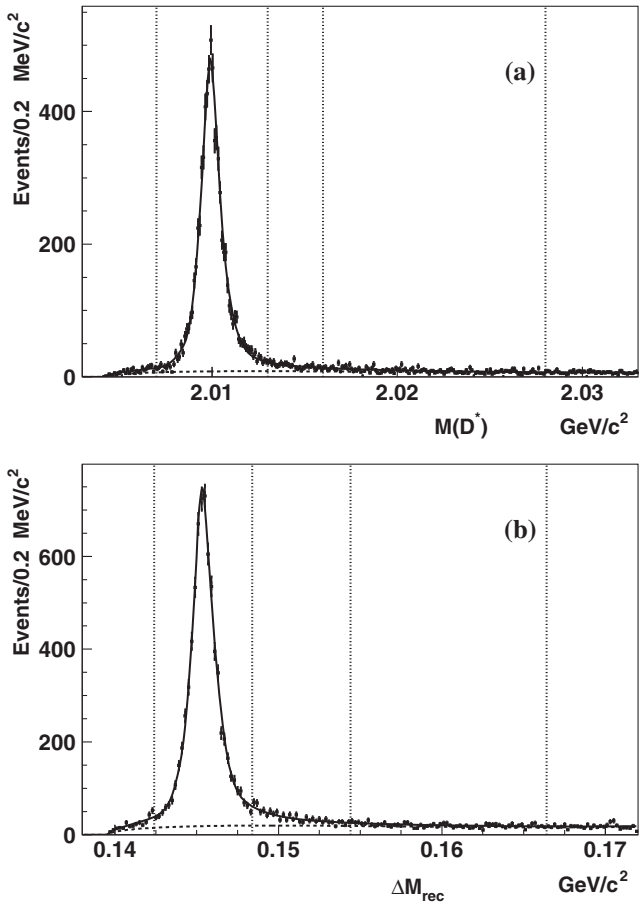

FIG. 6. Distributions of (a) $M(D^{*+})$ and (b) $\Delta M_{\rm rec}^{\rm fit}$. The solid line represents the result of the fit described in the text. The background contributions are shown as dotted curves. The signal and sideband regions are indicated by vertical lines.

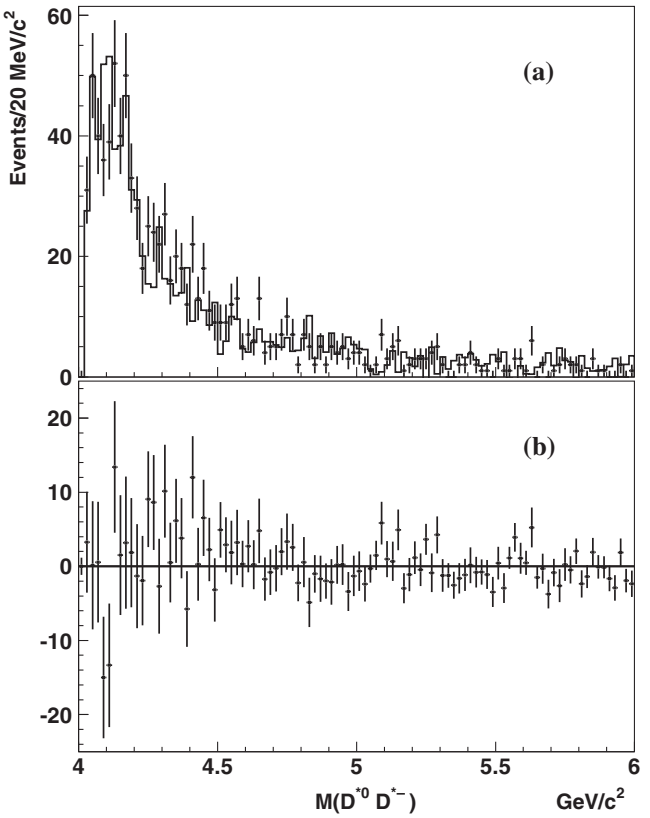

FIG. 7. The $M(D^{*0}D^{*-})$ spectrum after applying all requirements (a) before and (b) after combinatorial background subtraction. The solid histogram corresponds to the total contribution of the combinatorial background.

partial reconstruction method. Because of charge imbalance of the reconstructed combination $(D^{*0}\pi^-_{\rm slow}\gamma_{\rm ISR})$, only events with a missing $\pi^+_{\rm miss}$ can contribute to the recoil mass difference peak (indicating the presence of a D^{*-} meson). The $D^{*0}D^{*-}$ mass spectrum is obtained by applying all requirements and subtracting combinatorial backgrounds. To recalculate the background (4) contribution from the isospin-conjugated $M(D^{*0}D^{*-})$ spectrum, one needs to correct the latter for the ratio of the D^{*+} and D^{*0} reconstruction efficiencies (equal to 1.77, according to the MC) and the isospin factor $1/2$. As in the previous Belle analysis [13], this contribution is found to be consistent with 0 (Fig. 7). However, to avoid additional systematic errors, the spectrum of background (4) obtained from the data is subtracted bin by bin, and the statistical errors of the subtraction of this contribution are included in the final result.

The $D^{*+}D^{*-}$ mass spectrum after bin-by-bin combinatorial background subtraction is shown in Fig. 8.

Background (5) is also estimated from the data using the same method of partial reconstruction, substituting $\gamma_{\rm ISR}$ for a fully reconstructed energetic π^0. From the fit to the π^0 mass distribution, we find 56 ± 12 events corresponding to the process $e^+e^- \to D^{*+}D^{*-}\pi^0$ with $M(D^{*+}D^{*-}) \leq 6\ {\rm GeV}/c^2$. From the MC simulation, we estimate the ratio of efficiencies for background process (5) to be reconstructed as $D^{*+}D^{*-}\gamma_{\rm ISR}$ and $D^{*+}D^{*-}\pi^0$ to be equal to 0.39. Thus, we conclude that only 22 ± 5 events

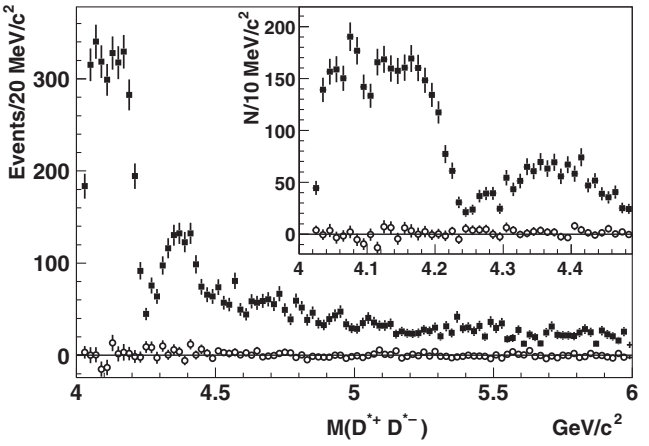

FIG. 8. The $M(D^{*+}D^{*-})$ spectrum after the combinatorial background (1)–(3) subtraction. The contribution from the process $e^+e^- \to D^{*+}D^{*-}\pi^0_{\rm miss}\gamma_{\rm ISR}$ is shown as open circles with error bars. The inset shows the spectrum near the threshold with finer bins.

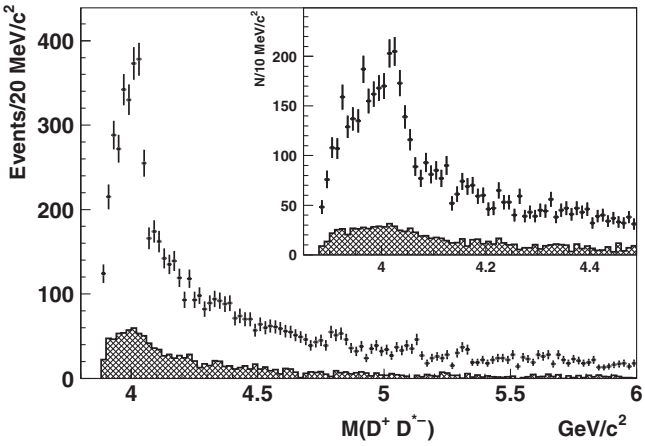

FIG. 9. The $M(D^+D^{*-})$ spectrum in the data after applying all selection criteria (points with error bars). The sum of backgrounds (1)–(3) is shown as the hatched histogram. The inset shows the spectrum near the threshold with finer bins.

contribute to our reconstructed ISR spectrum in the region $M(D^{*+}D^{*-}) \leq 6$ GeV$/c^2$, i.e., under 0.3% of the signal. As the $M(D^{*+}D^{*-})$ spectrum from $e^+e^- \to D^{*+}D^{*-}\pi^0$ is distributed uniformly, far less than one event per bin from this background is expected. Therefore, we incorporate this background contribution into the systematic uncertainty.

B. Measurement of $e^+e^- \to D^+D^{*-}\gamma_{\rm ISR}$

The D^+D^{*-} mass spectrum, after applying all the selection criteria, is shown in Fig. 9.

For $e^+e^- \to D^+D^{*-}\gamma_{\rm ISR}$, we consider similar background sources and use the same methods to subtract them:

(1) combinatorial D^+ candidate combined with a true slow pion from D^{*-} decay;
(2) real D^+ mesons combined with a combinatorial slow pion;
(3) both D^+ and $\pi^-_{\rm slow}$ are combinatorial;
(4a) reflection from the processes $e^+e^- \to D^+D^{*-}\pi^0_{\rm miss}\gamma_{\rm ISR}$ with a lost π^0 in the final state, including $e^+e^- \to D^{*+}D^{*-}\gamma_{\rm ISR}$ followed by $D^{*+} \to D^+\pi^0$;
(4b) reflection from $e^+e^- \to D^{*+}D^{*-}\gamma_{\rm ISR}$ followed by $D^{*+} \to D^+\gamma$;
(5) contribution from $e^+e^- \to D^+D^{*-}\pi^0_{\rm fast}$, where the fast $\pi^0_{\rm fast}$ is misidentified as $\gamma_{\rm ISR}$.

The contribution from the combinatorial backgrounds (1)–(3) is estimated using two-dimensional sideband regions of the D^+ candidate mass versus the recoil mass difference (Fig. 10).

The total contribution to the $M(D^+D^{*-})$ spectra of the combinatorial backgrounds (1)–(3) is calculated according to the formula

$$M_{\rm bg\,(1)–(3)} = 0.5 \cdot M_{\mathbf{B}} + 0.43 \cdot M_{\mathbf{C}} - 0.215 \cdot M_{\mathbf{D}}, \quad (6)$$

where $M_{\mathbf{B,C,D}}$ are the D^+D^{*-} mass spectra from the **B**, **C**, and **D** sidebands, respectively. The scaling factors are

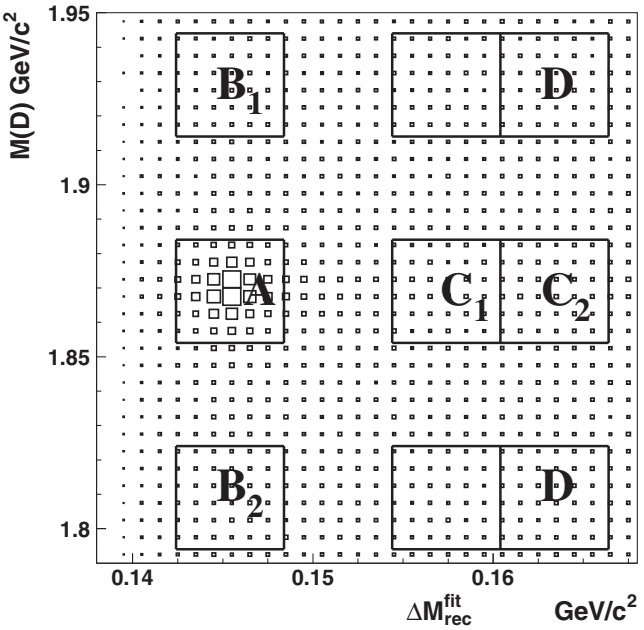

FIG. 10. The $M(D^+)$ vs $\Delta M^{\rm fit}_{\rm rec}$ scatter plot in the data.

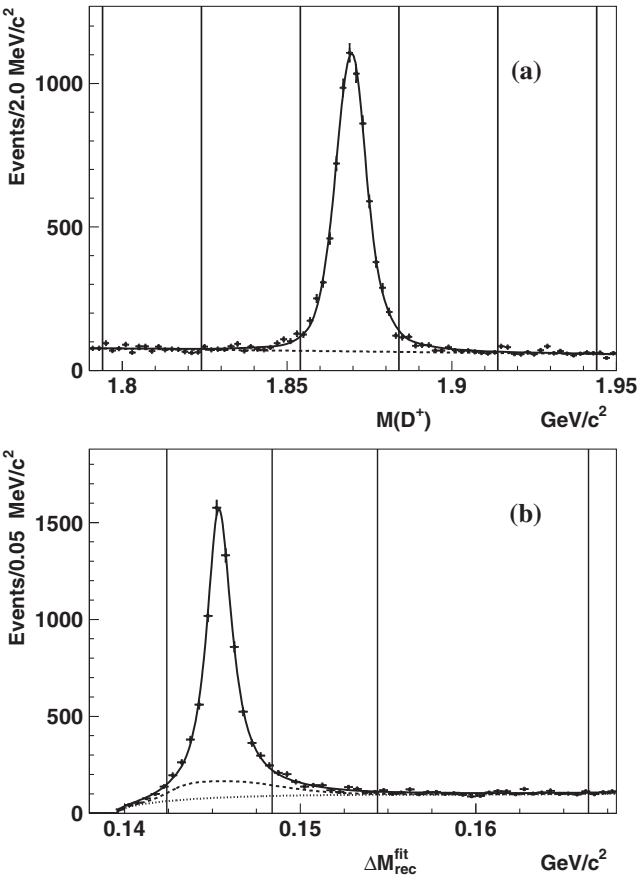

FIG. 11. Distributions of the (a) $M(D^+)$ and (b) $\Delta M^{\rm fit}_{\rm rec}$. The solid line represents the result of the fit described in the text. The combinatorial background contribution is shown as the dotted curve. The dashed curve corresponds to background (4). The signal and sidebands regions are indicated by vertical lines.

determined from the fits to the $M(D^+)$ and $\Delta M_{\rm rec}^{\rm fit}$ distributions shown in Fig. 11. In the case of the $M(D^+)$ sidebands, the scaling factor turns out to be exactly related to the ratio of widths for the sideband and signal windows, as the background is well described by a linear function. We note that background (4) contributes to the $\Delta M_{\rm rec}^{\rm fit}$ spectrum peak. However, this peak is wider than the signal's as the refitting procedure of the recoil mass against $D^{(*)+}\gamma_{\rm ISR}$ into the D^{*-} mass for this background process works improperly and does not improve the $\Delta M_{\rm rec}^{\rm fit}$ resolution. We fix this contribution [shown in Fig. 11(b) as the dashed-dotted line] from the MC.

To estimate the contribution of the background process (4a), the isospin-conjugated process $e^+e^- \to D^0D^{*-}\pi^+\gamma_{\rm ISR}$ is studied using the same method of partial reconstruction by replacing D^+ with D^0. Using the MC simulation, we verify that this method gives an accurate subtraction of the background without bias. The measured $M(D^0D^{*-})$ spectrum is shown in Fig. 12(a) as the points with error bars. We repeat the procedure of the subtraction of combinatorial background [shown by the hatched histogram in Fig. 12(a) similarly to the studied process] and obtain the net $M(D^0D^{*-})$ spectrum as shown in Fig. 12(b). The background process $e^+e^- \to D^+D^{*-}\pi^0\gamma_{\rm ISR}$ includes contributions from $e^+e^- \to D^{*+}D^{*-}\gamma_{\rm ISR}$ with $D^{*+} \to D^+\pi^0$ as well as higher resonance $D^{**+} \to D^+\pi^0_{\rm miss}$ or nonresonant

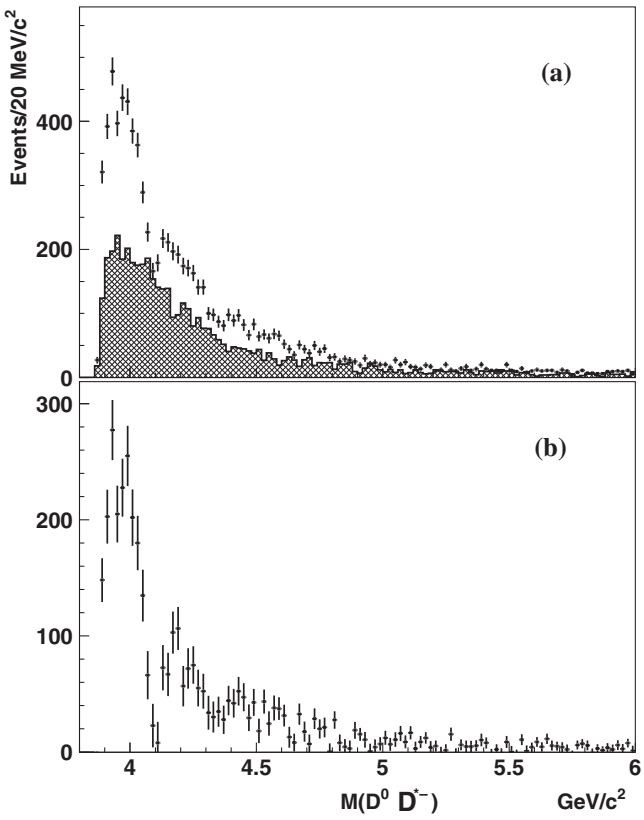

FIG. 12. The $M(D^0D^{*-})$ spectrum (a) before and (b) after subtraction of combinatorial background.

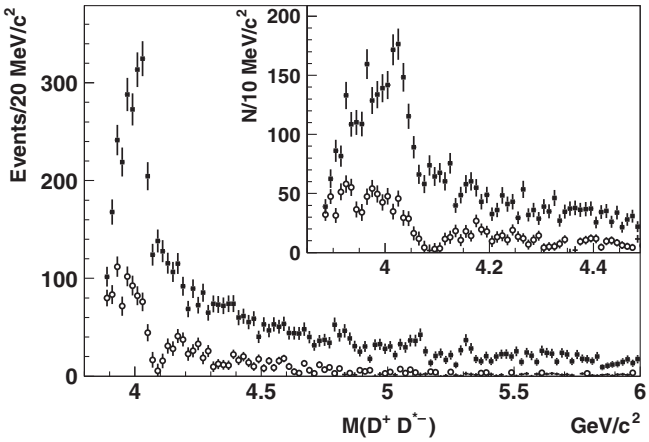

FIG. 13. The $M(D^+D^{*-})$ spectrum after subtraction of combinatorial background. Contribution from the $e^+e^- \to D^{*+}D^{*-}\gamma_{\rm ISR}$ is shown as open circles with error bars.

$D^+\pi^0_{\rm miss}$ contributions. For the two latter sources, the ratio $D^+\pi^0$ to $D^0\pi^+$ is related by the isospin factor $1/2$. A similar factor is valid for the ratio of $\mathcal{B}(D^{*+} \to D^+\pi^0)/\mathcal{B}(D^{*+} \to D^0\pi^+) = 0.453 \pm 0.011$ [1]. We do not study all of these contributions separately, but rather scale the measured D^0D^{*-} spectrum for the ratio of efficiencies for D^+ and D^0 (0.28 according to MC) and the factor 0.453, assuming the main contribution has $\pi^0_{\rm miss}$ coming from D^{*+}. The difference between $\mathcal{B}(D^{*+} \to D^+\pi^0)/\mathcal{B}(D^{*+} \to D^0\pi^+)$ and the isospin factor is taken into account in the systematic error of the result. The measured contribution from the process $e^+e^- \to D^+D^{*-}\pi^0\gamma_{\rm ISR}$ to the D^+D^{*-} mass spectrum is shown in Fig. 13 as the open circles.

The small contribution of background 4(b), from $e^+e^- \to D^{*+}D^{*-}\gamma_{\rm ISR}$ with $D^{*+} \to D^+\gamma$, is estimated using the MC simulation. In the $e^+e^- \to D^{*+}D^{*-}\gamma_{\rm ISR}$ MC sample, the $D^{*+}D^{*-}$ spectrum is set according to our measurement. Background 4(b) is tiny in comparison with 4(a) because of the small $\mathcal{B}(D^{*+} \to D^+\gamma)$ branching fraction and a greatly smeared $\Delta M_{\rm rec}^{\rm fit}$ distribution in the case of a lost γ.

Background (5) is estimated similarly to the study of $e^+e^- \to D^{*+}D^{*-}$ and found to be negligibly small. Its contribution is incorporated into the systematic uncertainty.

VII. ADDITIONAL CHECKS

We performed several checks to determine that the background subtraction procedure does not bias the measured spectra.

To verify that the combinatorial background subtraction is performed correctly, each of the **B** and **C** sideband regions is divided into two equal intervals: $\mathbf{B}_1$-$\mathbf{B}_2$ and $\mathbf{C}_1$-$\mathbf{C}_2$, respectively, as shown in Fig. 10. Then, the consistency of both the $M(D^{*+}D^{*-})$ shapes and normalizations in the pairs of subintervals is checked. The differences between these two pairs of control spectra are consistent with 0. The same

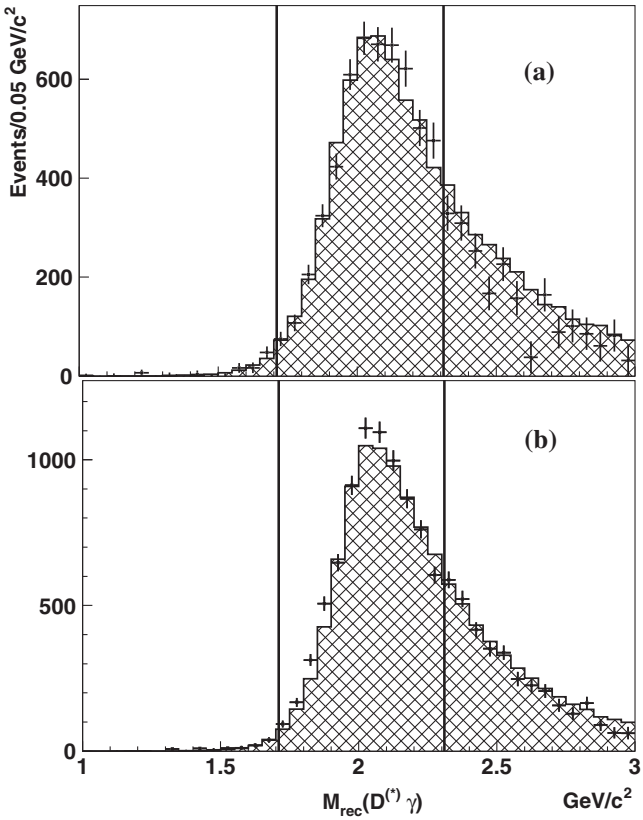

FIG. 14. (a) The $M_{\rm rec}(D^+\gamma_{\rm ISR})$ spectrum after subtraction of the combinatorial background and the contribution from the process $e^+e^- \to D^{*+}D^{*-}\gamma_{\rm ISR}$ for $e^+e^- \to D^+D^{*-}\gamma_{\rm ISR}$. (b) The $M_{\rm rec}(D^{*+}\gamma_{\rm ISR})$ spectrum after combinatorial-background subtraction for $e^+e^- \to D^{*+}D^{*-}\gamma_{\rm ISR}$. Points with error bars show the data after $\gamma_{\rm ISR}$ energy correction; the hatched histogram corresponds to the MC simulation. The signal window lies between the vertical lines.

procedure, repeated for the processes $e^+e^- \to D^+D^{*-}$, also demonstrates good agreement between the $M(D^+D^{*-})$ spectra from different sideband regions. We thus conclude that the combinatorial background shapes and normalizations are well understood.

We check that, after the energy correction of fast photons, the spectra of masses recoiling against $D^{(*)+}\gamma_{\rm ISR}$ combinations in the data are consistent with the MC expectations. Figures 14(a) and 14(b) show the $M_{\rm rec}(D^{(*)+}\gamma_{\rm ISR})$ spectra in the data (points with errors) and signal MC events (hatched histogram) for the processes $e^+e^- \to D^+D^{*-}\gamma_{\rm ISR}$ and $e^+e^- \to D^{*+}D^{*-}\gamma_{\rm ISR}$, respectively. The good agreement between MC and data spectra demonstrates not only the correctness of the photon energy calibration but also the proper background subtraction.

VIII. CROSS SECTION CALCULATION

We calculate the exclusive cross sections of the processes $e^+e^- \to D^+D^{*-}$ and $e^+e^- \to D^{*+}D^{*-}$ as a function of $\sqrt{s}$ according to the formula

$$\sigma_{e^+e^-\to D^{(*)+}D^{*-}} = \frac{dN/dM}{\eta_{\rm tot}(M)\cdot dL/dM}, \tag{7}$$

where M is the $D^{(*)+}D^{*-}$ mass, equivalent to $\sqrt{s}$, dN/dM is the measured mass spectrum, $\eta_{\rm tot}$ is an M-dependent total efficiency, and dL/dM is the differential luminosity.

The dependence of the efficiency on M is calculated using the MC simulation and is defined as the ratio of reconstructed mass spectrum for true MC candidates after applying all requirements to the generated spectrum (Fig. 15). Alternatively, we calculate the efficiency without the requirement that the selected MC candidates be the true combination, but repeating in this case the procedure of the background subtraction. The latter method checks for possible oversubtraction of the signal by the applied procedure of the combinatorial background subtraction due to tails in the $M(D^{*+})$ and recoil mass difference resolution functions. It is found that the oversubtraction is negligibly small, and both methods result in the same $\eta_{\rm tot}(M)$ dependence.

The differential luminosity is calculated as a sum over all energy points, $\Upsilon(4S)$, $\Upsilon(5S)$, and continuum, using the known luminosities of each data subsample. We use the dL/dM formula that includes the second-order QED corrections [29]. The latter varies from 2.5% to 3.5% of the leading contribution in the studied $\sqrt{s}$ interval. In the

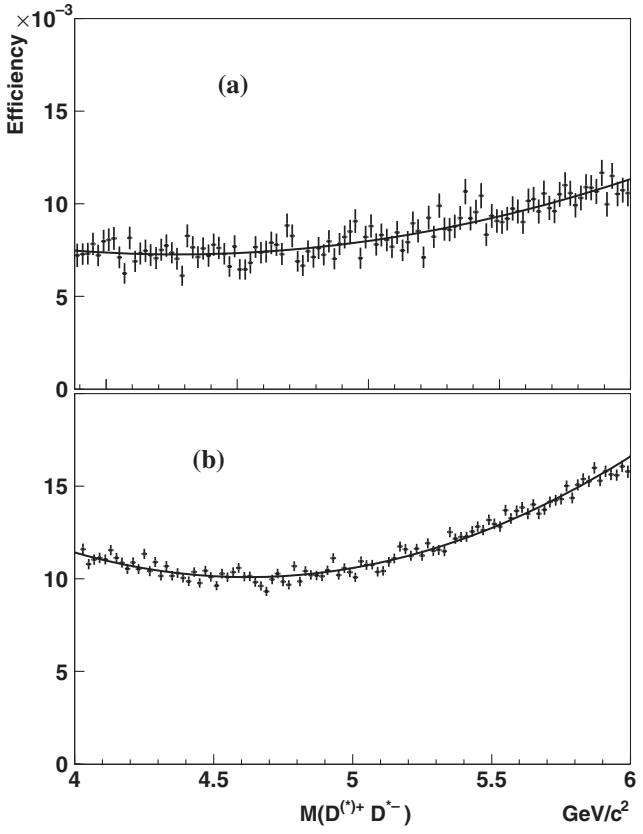

FIG. 15. The total efficiency, including the branching fractions, as a function of $M(D^{(*)+}D^{*-})$ for (a) $e^+e^- \to D^+D^{*-}\gamma_{\rm ISR}$ and (b) $e^+e^- \to D^{*+}D^{*-}\gamma_{\rm ISR}$.

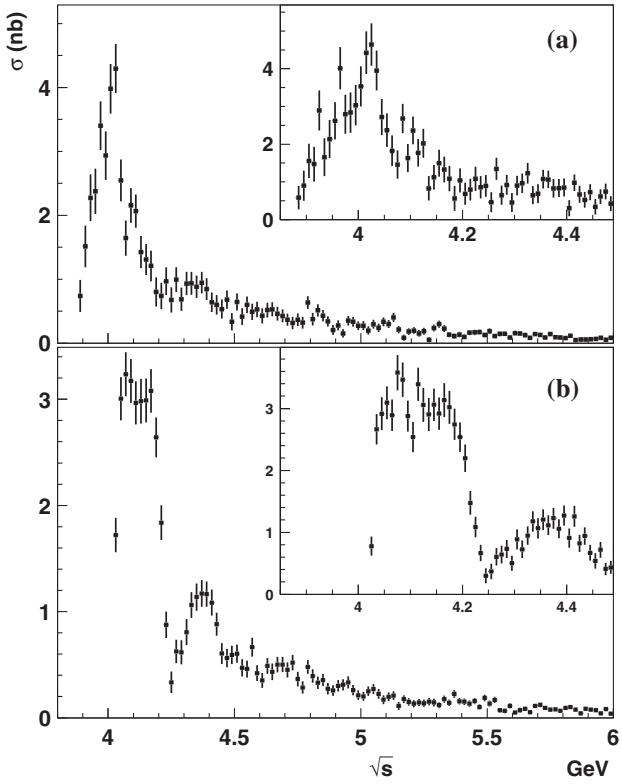

FIG. 16. The exclusive cross sections as functions of $\sqrt{s}$ for (a) $e^+e^- \to D^+D^{*-}$ and (b) $e^+e^- \to D^{*+}D^{*-}$.

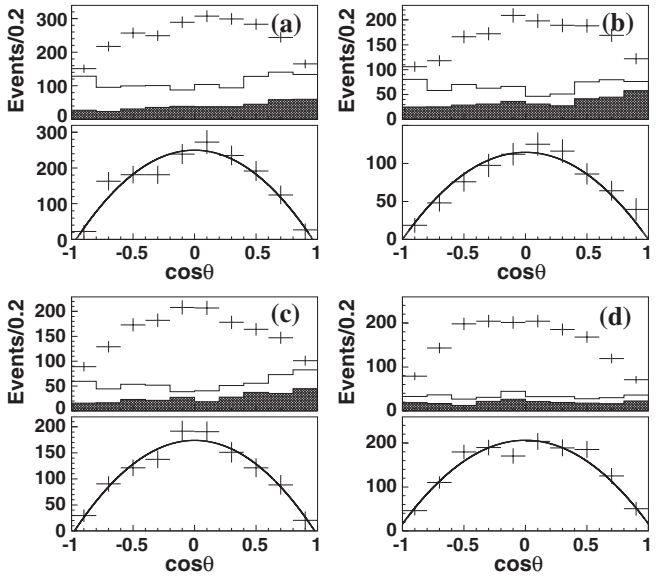

FIG. 17. The distribution of $\cos\theta$ before (top panels) and after (bottom panels) background subtraction for different mass range: (a) $M(D^+D^{*-}) < 4.05\,\mathrm{GeV}/c^2$, (b) $4.05\,\mathrm{GeV}/c^2 < M(D^+D^{*-}) < 4.3\,\mathrm{GeV}/c^2$, (c) $4.3\,\mathrm{GeV}/c^2 < M(D^+D^{*-}) < 4.8\,\mathrm{GeV}/c^2$, (d) $M(D^+D^{*-}) > 4.8\,\mathrm{GeV}/c^2$. The contribution from the combinatorial background only is shown as the hatched histogram. The total contribution from the background sources is shown as the open histogram.

previous Belle paper, this was treated as a systematic uncertainty.

Finally, the obtained exclusive $e^+e^- \to D^+D^{*-}$ and $e^+e^- \to D^{*+}D^{*-}$ cross sections are shown in Fig. 16.

IX. ANGULAR ANALYSIS OF D^+D^{*-} AND $D^{*+}D^{*-}$ FINAL STATES

We study the $D^{*\pm}$ helicities in both processes. The $D^{*\pm}$ helicity angle, θ, is defined as the angle between the $\pi^{\pm}_{\mathrm{slow}}$ from $D^{*\pm}$ decay and the $D^{(*)+}D^{*-}$ system, seen in the $D^{*\pm}$ rest frame. The angular distributions of the D^{*-} decays can be studied even in the case of partial D^{*-} reconstruction. The refit procedure of $M_{\mathrm{rec}}(D^{*+}\gamma_{\mathrm{ISR}})$ to $m_{D^{*-}}$ provides sufficient accuracy in the unreconstructed D^{*-} momentum determination. The helicity angle resolution of the partially reconstructed $D^{*\pm}$ mesons ($\sigma_\theta \sim 0.06$ rad) is slightly worse than for fully reconstructed $D^{*\pm}$ mesons ($\sigma_\theta \sim 0.05$ rad).

For the $e^+e^- \to D^+D^{*-}$ process, the helicity of the D^{*-} meson is uniquely defined by the angular momentum and parity conservation: the D^{*-} meson polarization should be transverse. Thus, we perform the D^{*-} angular analysis for this process to verify the method only.

The D^{*-} helicity angle distribution is analyzed in each bin of $M(D^+D^{*-})$. Figure 17 illustrates the obtained $\cos\theta$ distributions in different $M(D^+D^{*-})$ regions by combining several $M(D^+D^{*-})$ bins. Here, the combinatorial background contribution, taken from the $M(D^+)$ and $\Delta M^{\mathrm{fit}}_{\mathrm{rec}}$ sidebands, is shown as the hatched histogram, and the sum of the combinatorial background and $D^{*+}D^{*-}$ feed-down is shown as the open histogram; the latter contribution is obtained from the D^0D^- data, corrected for the D^0 and D^- efficiency ratio and the ratio of $\mathcal{B}(D^{*+} \to D^+\pi^0)/\mathcal{B}(D^{*+} \to D^0\pi^+)$. In each bin of $M(D^+D^{*-})$, the $\cos\theta$ distribution after subtraction of all background contributions is fitted with the function

$$F(\cos\theta) = \eta(\cos\theta) \cdot dM/dL \cdot (f_L + f_T), \qquad (8)$$

where $\eta(\cos\theta)$ is the efficiency depending on the helicity of the D^{*-}, dL/dM is calculated in each M bin, and $f_L = \sigma_L \cdot \cos^2\theta$ and $f_T = \sigma_T \cdot (1 - \cos^2\theta)$ are the contributions from distinct D^{*-} helicity states. The subscripts L and T refer to longitudinally and transversely polarized $D^{*\pm}$ mesons, correspondingly. The fitting procedure scans over M bins and the fits return the cross sections $\sigma_{T,L}(\sqrt{s})$ for T and L components. Figure 18 shows the resulting cross sections for $e^+e^- \to D^+D^{*-}_T$ and $D^+D^{*-}_L$. The latter is consistent with 0, as expected.

According to theoretical predictions for the processes $e^+e^- \to D^{*+}D^{*-}$ [30], the helicity composition of the $D^{*+}D^{*-}$ final state is a mixture of $D^*_TD^*_T$, $D^*_TD^*_L$ and $D^*_LD^*_L$. We perform a study of the $D^{*\pm}$ helicity angle distribution in each bin of $M(D^{*+}D^{*-})$.

We analyze the two-dimensional distribution of $c_1 \equiv \cos\theta_f$ vs $c_2 \equiv \cos\theta_p$, where the first helicity angle, θ_f,

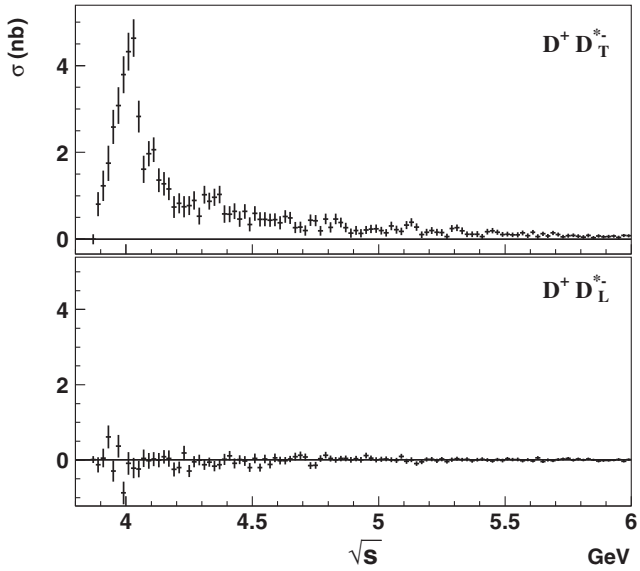

FIG. 18. The components of the $e^+e^- \to D^+D^{*-}\gamma_{\rm ISR}$ cross section corresponding to the different D^{*-} helicity: top is transverse; bottom is longitudinal.

corresponds to the fully reconstructed D^{*+}, and the second, θ_p, is calculated for the partially reconstructed D^{*-}. As an illustration, the two-dimensional distributions of c_1 versus c_2 for four mass ranges are shown in Fig. 19.

We perform binned maximum likelihood fits to these distributions in bins of $M(D^{*+}D^{*-})$. The fitting function is an incoherent sum of the LL and TL and TT contributions and the background component,

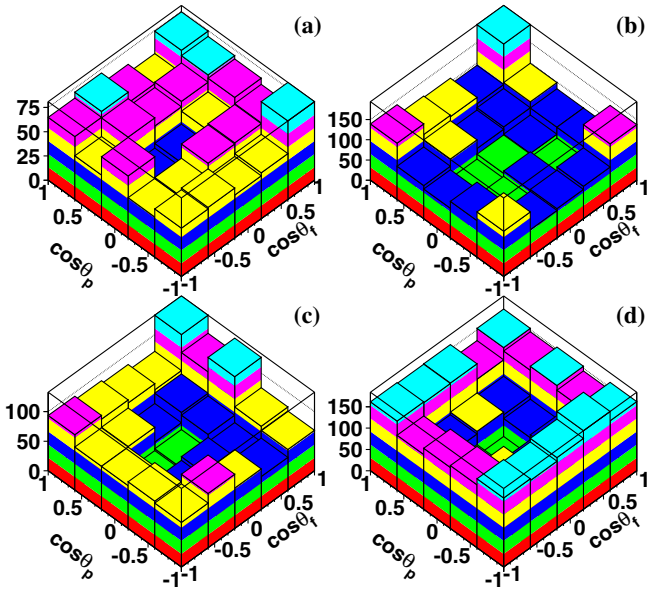

FIG. 19. Two-dimensional distribution of $\cos\theta_f$ vs $\cos\theta_p$ for different mass ranges: (a) 4.0 GeV/c^2 < $M(D^{*+}D^{*-})$ < 4.1 GeV/c^2, (b) 4.1 GeV/c^2 < $M(D^{*+}D^{*-})$ < 4.25 GeV/c^2, (c) 4.25 GeV/c^2 < $M(D^{*+}D^{*-})$ < 4.6 GeV/c^2, (d) $M(D^{*+}D^{*-})$ > 4.6 GeV/c^2.

$$f = \eta(c_1, c_2) \cdot dL/dM \cdot (f_{LL} + f_{TL} + f_{TT}) + f_{\rm bg}. \quad (9)$$

Here, $\eta(c_1, c_2)$ is the efficiency, depending on the two D^* helicity angles, and f_{LL}, f_{TL}, f_{TT}, and $f_{\rm bg}$ are the contributions from the three mutually orthogonal signal components and from the background, respectively. In this study, we take into account the combinatorial background only, and ignore the contributions of backgrounds (4) and (5) because they are very small. We define

$$\begin{aligned} f_{TT} &= \sigma_{TT} \cdot (1 - c_1^2) \cdot (1 - c_2^2), \\ f_{TL} &= \sigma_{TL} \cdot ((1 - c_1^2) \cdot c_2^2 + c_1^2 \cdot (1 - c_2^2)), \\ f_{LL} &= \sigma_{LL} \cdot c_1^2 \cdot c_2^2, \\ f_{\rm bg} &= N_{\rm bg}(0.58 \cdot f_{\mathbf{B}}(c_1, c_2) + 0.53 \cdot f_{\mathbf{C}}(c_1, c_2) \\ &\quad - 0.307 \cdot f_{\mathbf{D}}(c_1, c_2)), \end{aligned}$$

where σ_{LL}, σ_{TL}, and σ_{TT} are free parameters in the fit that represent the cross sections of each component in M bins. The $f_{\mathbf{B},\mathbf{C},\mathbf{D}}(c_1, c_2)$ are elements of the matrices that are constructed from the binned c_1 vs c_2 histograms for the

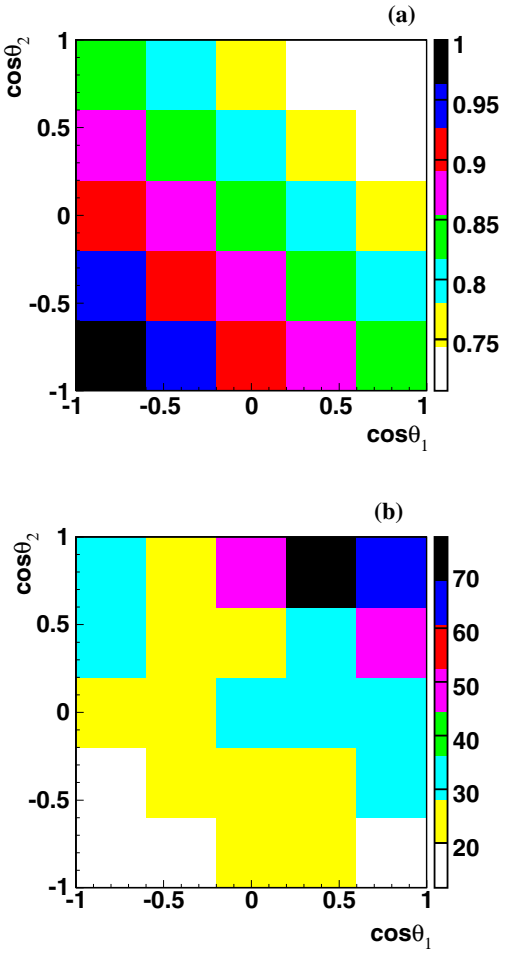

FIG. 20. The $e^+e^- \to D^{*+}D^{*-}\gamma_{\rm ISR}$ process: (a) reconstruction efficiency as a function c_1 and c_2 and (b) total combinatorial background distribution.

corresponding sideband regions; the background normalization, $N_{\rm bg}$, is fixed in each $M(D^{*+}D^{*-})$ bin within the error.

The efficiency map is shown in Fig. 20(a). The efficiency is almost symmetric with respect to c_1 vs c_2, as it depends mainly on the momenta of the two slow pions. The combinatorial background $f_{\rm bg}$ is presented in Fig. 20(b).

The angular-fit results are plotted in Fig. 21. We observe that the cross sections corresponding to the different $D^{*+}D^{*-}$ helicities have distinct dependencies on $\sqrt{s}$. Near the threshold, the TT and TL components have a similar sharp rise, while the LL component rises slowly. This can be explained by the high centrifugal barrier for the LL component, which originates from the F wave (chapter 48 of Ref. [1]). All three components reach the same value of ∼1 nb at $\sqrt{s} \sim 4.15$ GeV and fall into a common dip at $\sqrt{s} \sim 4.25$ GeV. The LL and TT components are attenuated and only the TL component survives in the region of high $\sqrt{s} \gtrsim 4.5$ GeV, which is in good agreement with theoretical predictions [31].

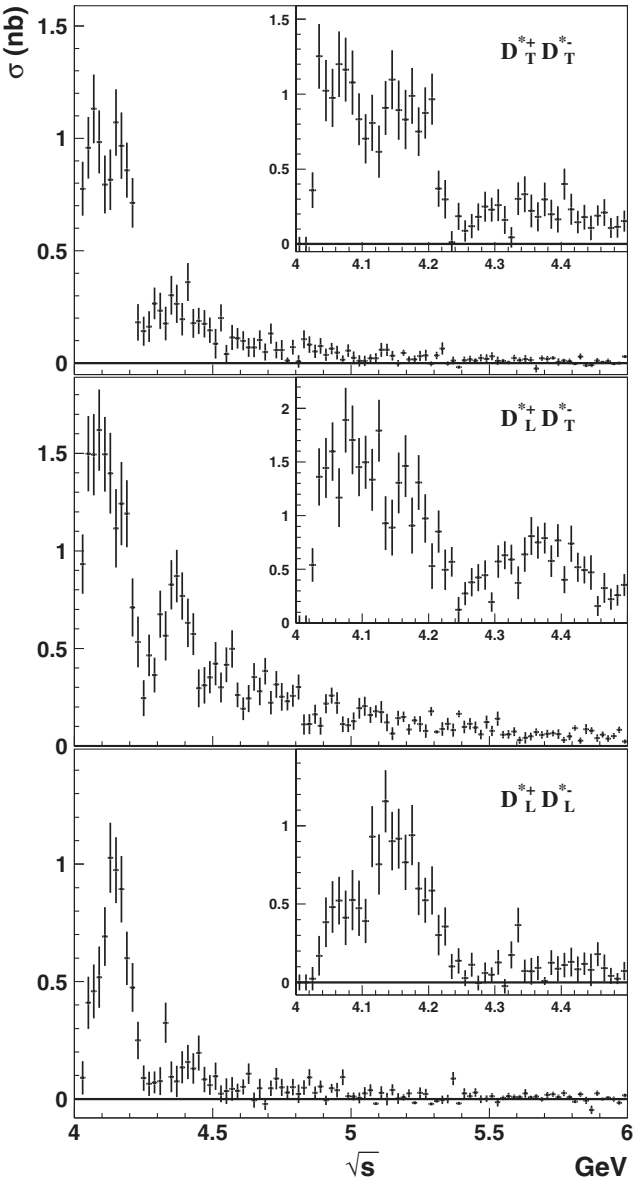

FIG. 21. The components of the $e^+e^- \to D^{*+}D^{*-}\gamma_{\rm ISR}$ cross section corresponding to the different $D^{*\pm}$'s helicities.

X. SYSTEMATIC ERRORS

The systematic errors in the cross section calculation for the studied processes are summarized in Table I.

The systematic errors arising from the background subtractions include the uncertainty in the calculation of the scaling factors for the sideband distributions in Eqs. (4) and (6), systematic errors in the determination of background (4) with missing neutrals and unsubtracted background (5). To estimate the uncertainty in the calculation of the scaling factors, we perform fits to Figs. 6 and 11 with different parametrizations and in different $M(D^{*+}D^{*-})$ intervals. As a result, the scaling factor extracted from the integral under the signal and sideband regions varies within ±15%. In spite of large uncertainties in this scaling factor, the final systematic error due to the subtraction of combinatorial backgrounds (1)–(3) is estimated to be only 2% as these backgrounds are small (only 15% of the signal). The systematic error associated with subtraction of background (4) includes the uncertainty of the isospin-conjugated spectra and efficiency ratio for the isospin-conjugated final states. The upper limit on background (5) is considered as an extra contribution to the systematic error.

The main contribution to the total systematic error comes from the uncertainties in track and photon reconstruction, estimated as 0.35% per track and 1.5% per photon. An extra uncertainty of 1% is ascribed to slow pion(s), and 2% to K^0_S reconstruction. Uncertainty of the kaon identification efficiency is 1%, evaluated by the study of inclusive D^* mesons.

The systematic error of the selection efficiency comes from the possible difference of resolution and calibration in the MC and data. Particularly, the calibration of the fast photon can influence the efficiency of the requirement $|M_{\rm rec}(D^{(*)+}\gamma_{\rm ISR}) - m_{D^{*-}}| < 300$ MeV/c^2. From the error in the photon energy correction factor obtained in our study, we estimate this uncertainty as ±1%. Other contributions are estimated by comparison of $M(D^{(*)})$ and $\Delta M^{\rm fit}_{\rm rec}$ distributions in the MC and data.

TABLE I. The summary of the systematic errors in the cross section calculation.

Source	D^+D^{*-}	$D^{*+}D^{*-}$
Background subtraction	2%	2%
Reconstruction	3%	4%
Selection	1%	1%
Angular distribution	-	2%
Cross section calculation	1.5%	1.5%
$\mathcal{B}(D^{(*)})$	2%	3%
MC statistics	1%	2%
Total	5%	7%

The uncertainty due to the D^* meson helicity distributions is reduced in comparison to the first Belle analysis [13], because the angular distributions are analyzed. We set the measured D^* helicity in the MC simulation to reduce the uncertainty of the slow pion reconstruction due to angular distribution in D^* decays.

The systematic error ascribed to the cross section calculation is estimated from a study of the $\cos\theta_0$ dependence (θ_0 defines the polar angle range for $\gamma_{\rm ISR}$ in the e^+e^- c.m. frame: $\theta_0 < \gamma_{\rm ISR} < 180° - \theta_0$) of the final result and includes a 1.4% error on the total luminosity. We add uncertainties of the same origin linearly, while independent uncertainties for different types of particles are summed quadratically. Different D modes have slightly different reconstruction uncertainties; the average error is calculated according to the weight of each mode in the final sample.

Other contributions come from the uncertainty in the absolute $D^{(*)}$ branching fractions [1] and from the MC statistics.

We divide the total systematic errors in two parts: correlated and uncorrelated.

The $\sqrt{s}$-independent correlated errors come from track reconstruction, selection efficiency, cross section calculation and uncertainty from the $D^{(*)}$ branching fractions. These errors influence the normalization of the measured cross section as a whole. Therefore, to take into account the correlated errors, the measured cross section should be multiplied by a factor of 1 ± 0.05 for $e^+e^- \to D^+D^{*-}$ and 1 ± 0.06 for $e^+e^- \to D^{*+}D^{*-}$.

On the contrary, the uncorrelated errors vary in each $\sqrt{s}$ bin. These errors come from the background subtraction (for $e^+e^- \to D^+D^{*-}$) and from calculating efficiency dependence on the helicity of the $D^{*+}D^{*-}$ final state (for $e^+e^- \to D^{*+}D^{*-}$). Uncorrelated systematic errors are given in Tables II and III.

XI. SUMMARY

In summary, we report measurements of the exclusive $e^+e^- \to D^+D^{*-}$ and $e^+e^- \to D^{*+}D^{*-}$ cross sections at $\sqrt{s}$ near D^+D^{*-} and $D^{*+}D^{*-}$ thresholds. These results supersede those of Ref. [13]. Due to the increased size of the data sample, an improved track reconstruction efficiency, and additional modes for the charmed meson reconstruction, the accuracy of the cross section measurements is increased by a factor of 2 compared to Ref. [13]. The systematic uncertainties are also significantly improved. We also extend the studied region up to $\sqrt{s} = 6$ GeV and, taking advantage of the improved resolution and high statistics, we halve the size of the $\sqrt{s}$ steps close to threshold.

The complex shape of the $e^+e^- \to D^{*+}D^{*-}$ cross sections can be explained by the fact that its components can interfere constructively or destructively. The fit of this cross section is not trivial, because it must take into account the threshold and coupled-channels effects [23].

The first angular analysis of the $e^+e^- \to D^{*+}D^{*-}$ process allows us to decompose the corresponding exclusive cross section into three possible components for the longitudinally, and transversely polarized $D^{*\pm}$ mesons. The obtained components have distinct behavior near the $D^{*+}D^{*-}$ threshold. The only nonvanishing component at higher energy is the TL helicity of the $D^{*+}D^{*-}$ final state. The measured decomposition allows the future measurement of the couplings of vector charmonium states into different helicity components, useful in identifying their nature and in testing the heavy-quark symmetry [32].

ACKNOWLEDGMENTS

We thank the KEKB group for the excellent operation of the accelerator; the KEK cryogenics group for the efficient operation of the solenoid; and the KEK computer group, the National Institute of Informatics, and the PNNL/EMSL computing group for valuable computing and SINET5 network support. We acknowledge support from the Ministry of Education, Culture, Sports, Science, and Technology (MEXT) of Japan, the Japan Society for the Promotion of Science (JSPS), and the Tau-Lepton Physics Research Center of Nagoya University; the Australian Research Council; Austrian Science Fund under Grant No. P 26794-N20; the National Natural Science Foundation of China under Contracts No. 10575109, No. 10775142, No. 10875115, No. 11175187, No. 11475187, No. 11521505 and No. 11575017; the Chinese Academy of Science Center for Excellence in Particle Physics; the Ministry of Education, Youth and Sports of the Czech Republic under Contract No. LG14034; the Carl Zeiss Foundation, the Deutsche Forschungsgemeinschaft, the Excellence Cluster Universe, and the VolkswagenStiftung; the Department of Science and Technology of India; the Istituto Nazionale di Fisica Nucleare of Italy; the WCU program of the Ministry of Education, National Research Foundation (NRF) of Korea Grants No. 2011-0029457, No. 2012-0008143, No. 2014R1A2A2A01005286, No. 2014R1A2A2A01002734, No. 2015R1A2A2A01003280, No. 2015H1A2A1033649, No. 2016R1D1A1B01010135, No. 2016K1A3A7A09005603, No. 2016K1A3A7A09005604, No. 2016R1D1A1B02012900, No. 2016K1A3A7A09005606, and No. NRF-2013K1A3A7A06056592; the Brain Korea 21-Plus program and Radiation Science Research Institute; the Polish Ministry of Science and Higher Education and the National Science Center; the Ministry of Education and Science of the Russian Federation under Contracts No. 3.2989.2017 and the Russian Foundation for Basic Research Grant No. 17-02-00485, No. 17-32-50019; the Slovenian Research Agency; Ikerbasque, Basque Foundation for Science and the Euskal Herriko Unibertsitatea (UPV/EHU) under program Grant No. UFI 11/55 (Spain); the Swiss National Science Foundation; the Ministry of Education and the Ministry of Science and Technology of Taiwan; and the U.S. Department of Energy and the National Science Foundation.

APPENDIX: THE VALUES OF THE CROSS SECTIONS

TABLE II. The values of the $e^+e^- \to D^+D^{*-}$ and $e^+e^- \to D^{*+}D^{*-}$ cross sections and their statistical and uncorrelated systematic errors. Correlated systematic errors equal to 5% and 6% for the $e^+e^- \to D^+D^{*-}$ and $e^+e^- \to D^{*+}D^{*-}$ process, respectively. The first tabulated error is statistical and the second is systematic.

$\sqrt{s}$ (GeV)	$\sigma_{e^+e^- \to D^+D^{*-}}$ (nb)	$\sigma_{e^+e^- \to D^{*+}D^{*-}}$ (nb)
3.875	$0.018 \pm 0.028 \pm 0.000$	
3.885	$0.579 \pm 0.312 \pm 0.022$	
3.895	$0.898 \pm 0.396 \pm 0.036$	
3.905	$1.556 \pm 0.457 \pm 0.045$	
3.915	$1.470 \pm 0.461 \pm 0.046$	
3.925	$2.893 \pm 0.533 \pm 0.054$	
3.935	$1.654 \pm 0.500 \pm 0.057$	
3.945	$2.135 \pm 0.507 \pm 0.053$	
3.955	$2.617 \pm 0.494 \pm 0.042$	
3.965	$4.014 \pm 0.561 \pm 0.049$	
3.975	$2.796 \pm 0.518 \pm 0.051$	
3.985	$2.837 \pm 0.535 \pm 0.055$	
3.995	$3.030 \pm 0.536 \pm 0.055$	
4.005	$3.532 \pm 0.529 \pm 0.046$	
4.015	$4.424 \pm 0.566 \pm 0.050$	
4.025	$4.642 \pm 0.561 \pm 0.047$	$0.788 \pm 0.156 \pm 0.025$
4.035	$3.953 \pm 0.526 \pm 0.038$	$2.702 \pm 0.249 \pm 0.085$
4.045	$2.719 \pm 0.479 \pm 0.040$	$2.958 \pm 0.272 \pm 0.094$
4.055	$2.372 \pm 0.445 \pm 0.031$	$3.137 \pm 0.268 \pm 0.101$
4.065	$1.825 \pm 0.404 \pm 0.023$	$2.932 \pm 0.260 \pm 0.096$
4.075	$1.460 \pm 0.379 \pm 0.022$	$3.629 \pm 0.290 \pm 0.120$
4.085	$2.681 \pm 0.391 \pm 0.009$	$3.514 \pm 0.281 \pm 0.117$
4.095	$1.629 \pm 0.374 \pm 0.021$	$2.919 \pm 0.254 \pm 0.098$
4.105	$2.364 \pm 0.369 \pm 0.009$	$2.574 \pm 0.251 \pm 0.087$
4.115	$1.768 \pm 0.365 \pm 0.016$	$3.436 \pm 0.271 \pm 0.118$
4.125	$2.022 \pm 0.383 \pm 0.019$	$3.100 \pm 0.278 \pm 0.107$
4.135	$0.828 \pm 0.324 \pm 0.018$	$2.943 \pm 0.270 \pm 0.103$
4.145	$1.122 \pm 0.329 \pm 0.018$	$3.102 \pm 0.264 \pm 0.109$
4.155	$1.492 \pm 0.357 \pm 0.018$	$2.956 \pm 0.266 \pm 0.105$
4.165	$1.327 \pm 0.341 \pm 0.018$	$3.178 \pm 0.277 \pm 0.114$
4.175	$1.087 \pm 0.338 \pm 0.024$	$3.060 \pm 0.269 \pm 0.110$
4.185	$0.562 \pm 0.329 \pm 0.027$	$2.780 \pm 0.255 \pm 0.101$
4.195	$1.038 \pm 0.321 \pm 0.018$	$2.570 \pm 0.240 \pm 0.094$
4.205	$0.683 \pm 0.294 \pm 0.016$	$2.226 \pm 0.226 \pm 0.082$
4.215	$0.793 \pm 0.290 \pm 0.014$	$1.495 \pm 0.193 \pm 0.056$
4.225	$1.081 \pm 0.321 \pm 0.020$	$1.100 \pm 0.168 \pm 0.041$
4.235	$0.856 \pm 0.297 \pm 0.016$	$0.674 \pm 0.133 \pm 0.025$
4.245	$0.894 \pm 0.290 \pm 0.016$	$0.303 \pm 0.122 \pm 0.011$
4.255	$0.460 \pm 0.267 \pm 0.016$	$0.374 \pm 0.126 \pm 0.014$
4.265	$1.344 \pm 0.293 \pm 0.010$	$0.614 \pm 0.141 \pm 0.024$
4.275	$0.647 \pm 0.254 \pm 0.011$	$0.650 \pm 0.146 \pm 0.025$
4.285	$0.920 \pm 0.261 \pm 0.008$	$0.741 \pm 0.147 \pm 0.029$
4.295	$0.452 \pm 0.252 \pm 0.015$	$0.507 \pm 0.124 \pm 0.020$
4.305	$0.903 \pm 0.258 \pm 0.010$	$0.897 \pm 0.165 \pm 0.035$
4.315	$0.961 \pm 0.256 \pm 0.008$	$0.735 \pm 0.143 \pm 0.029$
4.325	$1.228 \pm 0.273 \pm 0.010$	$0.959 \pm 0.149 \pm 0.038$
4.335	$0.646 \pm 0.237 \pm 0.010$	$1.191 \pm 0.167 \pm 0.047$
4.345	$0.688 \pm 0.250 \pm 0.014$	$1.078 \pm 0.165 \pm 0.043$
4.355	$1.074 \pm 0.249 \pm 0.007$	$1.221 \pm 0.169 \pm 0.049$
4.365	$1.064 \pm 0.233 \pm 0.003$	$1.127 \pm 0.162 \pm 0.045$
4.375	$0.829 \pm 0.245 \pm 0.012$	$1.241 \pm 0.169 \pm 0.050$
4.385	$0.837 \pm 0.241 \pm 0.009$	$1.069 \pm 0.153 \pm 0.043$
4.395	$0.852 \pm 0.242 \pm 0.010$	$1.285 \pm 0.163 \pm 0.052$
4.405	$0.299 \pm 0.213 \pm 0.013$	$0.919 \pm 0.157 \pm 0.037$
4.415	$0.979 \pm 0.220 \pm 0.003$	$1.272 \pm 0.172 \pm 0.051$
4.425	$0.670 \pm 0.221 \pm 0.010$	$0.831 \pm 0.141 \pm 0.034$
4.435	$0.525 \pm 0.211 \pm 0.009$	$0.951 \pm 0.143 \pm 0.039$
4.445	$0.728 \pm 0.213 \pm 0.007$	$0.677 \pm 0.129 \pm 0.028$
4.455	$0.340 \pm 0.207 \pm 0.012$	$0.545 \pm 0.127 \pm 0.022$
4.465	$0.612 \pm 0.195 \pm 0.006$	$0.725 \pm 0.128 \pm 0.030$
4.475	$0.745 \pm 0.211 \pm 0.007$	$0.412 \pm 0.102 \pm 0.017$
4.485	$0.423 \pm 0.197 \pm 0.009$	$0.440 \pm 0.107 \pm 0.018$
4.495	$0.248 \pm 0.185 \pm 0.010$	$0.754 \pm 0.121 \pm 0.031$
4.505	$0.725 \pm 0.200 \pm 0.006$	$0.635 \pm 0.115 \pm 0.026$
4.515	$0.564 \pm 0.179 \pm 0.004$	$0.584 \pm 0.119 \pm 0.024$
4.525	$0.295 \pm 0.176 \pm 0.009$	$0.573 \pm 0.104 \pm 0.023$
4.535	$0.535 \pm 0.192 \pm 0.008$	$0.378 \pm 0.105 \pm 0.015$
4.545	$0.757 \pm 0.194 \pm 0.005$	$0.652 \pm 0.119 \pm 0.027$
4.555	$0.439 \pm 0.174 \pm 0.006$	$0.275 \pm 0.091 \pm 0.011$
4.565	$0.519 \pm 0.185 \pm 0.007$	$0.566 \pm 0.121 \pm 0.023$
4.575	$0.460 \pm 0.179 \pm 0.007$	$0.776 \pm 0.124 \pm 0.031$
4.585	$0.464 \pm 0.173 \pm 0.007$	$0.452 \pm 0.096 \pm 0.018$
4.595	$0.593 \pm 0.170 \pm 0.004$	$0.396 \pm 0.091 \pm 0.016$
4.605	$0.506 \pm 0.178 \pm 0.007$	$0.323 \pm 0.088 \pm 0.013$
4.615	$0.351 \pm 0.157 \pm 0.006$	$0.387 \pm 0.094 \pm 0.016$
4.625	$0.474 \pm 0.158 \pm 0.004$	$0.507 \pm 0.101 \pm 0.020$
4.635	$0.558 \pm 0.171 \pm 0.005$	$0.479 \pm 0.098 \pm 0.019$
4.645	$0.333 \pm 0.145 \pm 0.004$	$0.438 \pm 0.103 \pm 0.017$
4.655	$0.724 \pm 0.162 \pm 0.001$	$0.434 \pm 0.103 \pm 0.017$
4.665	$0.460 \pm 0.152 \pm 0.003$	$0.456 \pm 0.097 \pm 0.018$
4.675	$0.460 \pm 0.147 \pm 0.004$	$0.551 \pm 0.096 \pm 0.022$
4.685	$0.485 \pm 0.152 \pm 0.004$	$0.357 \pm 0.088 \pm 0.014$
4.695	$0.365 \pm 0.136 \pm 0.003$	$0.653 \pm 0.106 \pm 0.025$
4.705	$0.312 \pm 0.132 \pm 0.003$	$0.391 \pm 0.093 \pm 0.015$
4.715	$0.419 \pm 0.137 \pm 0.002$	$0.517 \pm 0.093 \pm 0.020$
4.725	$0.303 \pm 0.137 \pm 0.004$	$0.481 \pm 0.098 \pm 0.018$
4.735	$0.327 \pm 0.138 \pm 0.005$	$0.565 \pm 0.102 \pm 0.022$
4.745	$0.301 \pm 0.129 \pm 0.003$	$0.481 \pm 0.101 \pm 0.018$
4.755	$0.430 \pm 0.148 \pm 0.004$	$0.254 \pm 0.078 \pm 0.010$
4.765	$0.155 \pm 0.112 \pm 0.003$	$0.255 \pm 0.081 \pm 0.010$
4.775	$0.482 \pm 0.144 \pm 0.003$	$0.320 \pm 0.076 \pm 0.012$
4.785	$0.846 \pm 0.159 \pm 0.001$	$0.498 \pm 0.091 \pm 0.018$
4.795	$0.427 \pm 0.119 \pm 0.000$	$0.465 \pm 0.088 \pm 0.017$
4.805	$0.439 \pm 0.145 \pm 0.005$	$0.392 \pm 0.090 \pm 0.014$
4.815	$0.310 \pm 0.129 \pm 0.004$	$0.399 \pm 0.084 \pm 0.014$
4.825	$0.397 \pm 0.127 \pm 0.003$	$0.237 \pm 0.073 \pm 0.008$
4.835	$0.628 \pm 0.146 \pm 0.002$	$0.426 \pm 0.079 \pm 0.015$
4.845	$0.416 \pm 0.128 \pm 0.003$	$0.374 \pm 0.082 \pm 0.013$
4.855	$0.443 \pm 0.125 \pm 0.001$	$0.341 \pm 0.074 \pm 0.012$
4.865	$0.368 \pm 0.114 \pm 0.001$	$0.229 \pm 0.073 \pm 0.008$
4.875	$0.311 \pm 0.114 \pm 0.002$	$0.319 \pm 0.070 \pm 0.011$

(Table continued)

TABLE II. *(Continued)*

$\sqrt{s}$ (GeV)	$\sigma_{e^+e^-\to D^+D^{*-}}$ (nb)	$\sigma_{e^+e^-\to D^{*+}D^{*-}}$ (nb)
4.885	$0.226 \pm 0.106 \pm 0.002$	$0.158 \pm 0.054 \pm 0.005$
4.895	$0.187 \pm 0.110 \pm 0.004$	$0.357 \pm 0.074 \pm 0.012$
4.905	$0.225 \pm 0.104 \pm 0.003$	$0.384 \pm 0.073 \pm 0.013$
4.915	$0.330 \pm 0.118 \pm 0.003$	$0.222 \pm 0.072 \pm 0.007$
4.925	$0.169 \pm 0.083 \pm 0.001$	$0.273 \pm 0.068 \pm 0.009$
4.935	$0.135 \pm 0.104 \pm 0.004$	$0.351 \pm 0.076 \pm 0.011$
4.945	$0.341 \pm 0.110 \pm 0.002$	$0.328 \pm 0.069 \pm 0.010$
4.955	$0.359 \pm 0.098 \pm 0.000$	$0.343 \pm 0.081 \pm 0.011$
4.965	$0.334 \pm 0.118 \pm 0.003$	$0.293 \pm 0.066 \pm 0.009$
4.975	$0.338 \pm 0.098 \pm 0.000$	$0.229 \pm 0.063 \pm 0.007$
4.985	$0.347 \pm 0.104 \pm 0.001$	$0.257 \pm 0.061 \pm 0.008$
4.995	$0.197 \pm 0.090 \pm 0.002$	$0.170 \pm 0.058 \pm 0.005$
5.005	$0.215 \pm 0.093 \pm 0.002$	$0.233 \pm 0.061 \pm 0.007$
5.015	$0.330 \pm 0.101 \pm 0.001$	$0.172 \pm 0.055 \pm 0.005$
5.025	$0.113 \pm 0.078 \pm 0.002$	$0.260 \pm 0.060 \pm 0.007$
5.035	$0.281 \pm 0.099 \pm 0.002$	$0.244 \pm 0.061 \pm 0.007$
5.045	$0.300 \pm 0.095 \pm 0.001$	$0.282 \pm 0.065 \pm 0.008$
5.055	$0.289 \pm 0.103 \pm 0.002$	$0.261 \pm 0.062 \pm 0.007$
5.065	$0.264 \pm 0.093 \pm 0.002$	$0.185 \pm 0.054 \pm 0.005$
5.075	$0.212 \pm 0.093 \pm 0.002$	$0.265 \pm 0.062 \pm 0.007$
5.085	$0.334 \pm 0.095 \pm 0.001$	$0.160 \pm 0.053 \pm 0.004$
5.095	$0.330 \pm 0.098 \pm 0.001$	$0.182 \pm 0.063 \pm 0.004$
5.105	$0.311 \pm 0.097 \pm 0.002$	$0.178 \pm 0.055 \pm 0.004$
5.115	$0.283 \pm 0.082 \pm 0.000$	$0.221 \pm 0.057 \pm 0.005$
5.125	$0.438 \pm 0.104 \pm 0.001$	$0.250 \pm 0.061 \pm 0.006$
5.135	$0.364 \pm 0.098 \pm 0.001$	$0.170 \pm 0.053 \pm 0.004$
5.145	$0.262 \pm 0.086 \pm 0.001$	$0.183 \pm 0.055 \pm 0.004$
5.155	$0.163 \pm 0.073 \pm 0.001$	$0.042 \pm 0.042 \pm 0.001$
5.165	$0.142 \pm 0.073 \pm 0.001$	$0.108 \pm 0.043 \pm 0.002$
5.175	$0.028 \pm 0.063 \pm 0.002$	$0.245 \pm 0.053 \pm 0.005$
5.185	$0.204 \pm 0.071 \pm 0.000$	$0.220 \pm 0.054 \pm 0.004$
5.195	$0.158 \pm 0.076 \pm 0.002$	$0.080 \pm 0.036 \pm 0.002$
5.205	$0.240 \pm 0.083 \pm 0.001$	$0.196 \pm 0.050 \pm 0.004$
5.215	$0.155 \pm 0.064 \pm 0.000$	$0.070 \pm 0.038 \pm 0.001$
5.225	$0.081 \pm 0.066 \pm 0.002$	$0.121 \pm 0.046 \pm 0.002$
5.235	$0.223 \pm 0.078 \pm 0.001$	$0.166 \pm 0.044 \pm 0.003$
5.245	$0.152 \pm 0.075 \pm 0.002$	$0.149 \pm 0.051 \pm 0.002$
5.255	$0.225 \pm 0.077 \pm 0.001$	$0.126 \pm 0.042 \pm 0.002$
5.265	$0.038 \pm 0.063 \pm 0.002$	$0.108 \pm 0.042 \pm 0.002$
5.275	$0.064 \pm 0.054 \pm 0.001$	$0.197 \pm 0.049 \pm 0.003$
5.285	$0.286 \pm 0.080 \pm 0.001$	$0.142 \pm 0.048 \pm 0.002$
5.295	$0.184 \pm 0.068 \pm 0.000$	$0.145 \pm 0.047 \pm 0.002$
5.305	$0.342 \pm 0.080 \pm 0.000$	$0.070 \pm 0.032 \pm 0.001$
5.315	$0.251 \pm 0.076 \pm 0.001$	$0.169 \pm 0.045 \pm 0.002$
5.325	$0.185 \pm 0.077 \pm 0.002$	$0.153 \pm 0.043 \pm 0.002$
5.335	$0.265 \pm 0.078 \pm 0.001$	$0.199 \pm 0.047 \pm 0.002$
5.345	$0.178 \pm 0.058 \pm 0.000$	$0.179 \pm 0.044 \pm 0.002$
5.355	$0.084 \pm 0.058 \pm 0.001$	$0.104 \pm 0.036 \pm 0.001$
5.365	$0.143 \pm 0.056 \pm 0.000$	$0.245 \pm 0.051 \pm 0.002$
5.375	$0.074 \pm 0.060 \pm 0.002$	$0.205 \pm 0.050 \pm 0.002$
5.385	$0.135 \pm 0.064 \pm 0.001$	$0.201 \pm 0.047 \pm 0.002$
5.395	$0.133 \pm 0.057 \pm 0.001$	$0.112 \pm 0.037 \pm 0.001$
5.405	$0.087 \pm 0.052 \pm 0.001$	$0.156 \pm 0.041 \pm 0.001$
5.415	$0.109 \pm 0.058 \pm 0.001$	$0.147 \pm 0.044 \pm 0.001$
5.425	$0.166 \pm 0.054 \pm 0.000$	$0.134 \pm 0.039 \pm 0.001$
5.435	$0.160 \pm 0.062 \pm 0.001$	$0.133 \pm 0.038 \pm 0.001$
5.445	$0.169 \pm 0.057 \pm 0.000$	$0.152 \pm 0.041 \pm 0.001$
5.455	$0.165 \pm 0.060 \pm 0.001$	$0.165 \pm 0.041 \pm 0.001$
5.465	$0.180 \pm 0.057 \pm 0.000$	$0.066 \pm 0.029 \pm 0.000$
5.475	$0.170 \pm 0.057 \pm 0.000$	$0.138 \pm 0.038 \pm 0.000$
5.485	$0.168 \pm 0.054 \pm 0.000$	$0.192 \pm 0.042 \pm 0.000$
5.495	$0.086 \pm 0.057 \pm 0.002$	$0.181 \pm 0.043 \pm 0.000$
5.505	$0.158 \pm 0.055 \pm 0.000$	$0.158 \pm 0.039 \pm 0.000$
5.515	$0.215 \pm 0.067 \pm 0.001$	$0.110 \pm 0.037 \pm 0.000$
5.525	$0.100 \pm 0.041 \pm 0.000$	$0.176 \pm 0.042 \pm 0.000$
5.535	$0.120 \pm 0.042 \pm 0.000$	$0.163 \pm 0.039 \pm 0.000$
5.545	$0.148 \pm 0.058 \pm 0.001$	$0.072 \pm 0.028 \pm 0.000$
5.555	$0.140 \pm 0.051 \pm 0.000$	$0.074 \pm 0.030 \pm 0.000$
5.565	$0.173 \pm 0.055 \pm 0.000$	$0.042 \pm 0.028 \pm 0.000$
5.575	$0.117 \pm 0.049 \pm 0.000$	$0.089 \pm 0.032 \pm 0.000$
5.585	$0.103 \pm 0.052 \pm 0.001$	$0.069 \pm 0.030 \pm 0.000$
5.595	$0.075 \pm 0.045 \pm 0.001$	$0.156 \pm 0.038 \pm 0.001$
5.605	$0.104 \pm 0.050 \pm 0.001$	$0.039 \pm 0.021 \pm 0.000$
5.615	$0.206 \pm 0.059 \pm 0.000$	$0.063 \pm 0.026 \pm 0.000$
5.625	$0.100 \pm 0.047 \pm 0.001$	$0.035 \pm 0.025 \pm 0.000$
5.635	$0.199 \pm 0.056 \pm 0.000$	$0.106 \pm 0.037 \pm 0.001$
5.645	$0.173 \pm 0.058 \pm 0.001$	$0.077 \pm 0.026 \pm 0.001$
5.655	$0.078 \pm 0.050 \pm 0.001$	$0.094 \pm 0.029 \pm 0.001$
5.665	$0.075 \pm 0.040 \pm 0.000$	$0.051 \pm 0.021 \pm 0.000$
5.675	$0.092 \pm 0.046 \pm 0.001$	$0.055 \pm 0.026 \pm 0.001$
5.685	$0.104 \pm 0.049 \pm 0.001$	$0.123 \pm 0.032 \pm 0.001$
5.695	$0.177 \pm 0.054 \pm 0.001$	$0.098 \pm 0.028 \pm 0.001$
5.705	$0.130 \pm 0.047 \pm 0.000$	$0.142 \pm 0.034 \pm 0.002$
5.715	$0.127 \pm 0.043 \pm 0.000$	$0.102 \pm 0.030 \pm 0.001$
5.725	$0.157 \pm 0.049 \pm 0.000$	$0.085 \pm 0.029 \pm 0.001$
5.735	$0.020 \pm 0.030 \pm 0.001$	$0.102 \pm 0.028 \pm 0.001$
5.745	$0.097 \pm 0.040 \pm 0.000$	$0.059 \pm 0.025 \pm 0.001$
5.755	$0.182 \pm 0.047 \pm 0.000$	$0.097 \pm 0.028 \pm 0.001$
5.765	$0.111 \pm 0.045 \pm 0.001$	$0.088 \pm 0.029 \pm 0.001$
5.775	$0.076 \pm 0.041 \pm 0.001$	$0.071 \pm 0.023 \pm 0.001$
5.785	$0.124 \pm 0.044 \pm 0.000$	$0.055 \pm 0.025 \pm 0.001$
5.795	$0.049 \pm 0.032 \pm 0.000$	$0.078 \pm 0.025 \pm 0.001$
5.805	$0.043 \pm 0.036 \pm 0.001$	$0.103 \pm 0.028 \pm 0.002$
5.815	$0.111 \pm 0.043 \pm 0.001$	$0.085 \pm 0.025 \pm 0.002$
5.825	$0.064 \pm 0.034 \pm 0.000$	$0.088 \pm 0.026 \pm 0.002$
5.835	$0.167 \pm 0.045 \pm 0.000$	$0.114 \pm 0.028 \pm 0.002$
5.845	$0.048 \pm 0.032 \pm 0.000$	$0.058 \pm 0.021 \pm 0.001$
5.855	$0.042 \pm 0.034 \pm 0.001$	$0.095 \pm 0.029 \pm 0.002$
5.865	$0.072 \pm 0.032 \pm 0.000$	$0.041 \pm 0.019 \pm 0.001$
5.875	$0.040 \pm 0.032 \pm 0.001$	$0.041 \pm 0.018 \pm 0.001$
5.885	$0.046 \pm 0.033 \pm 0.001$	$0.103 \pm 0.027 \pm 0.002$
5.895	$0.070 \pm 0.031 \pm 0.000$	$0.070 \pm 0.022 \pm 0.002$
5.905	$-0.013 \pm 0.025 \pm 0.001$	$0.080 \pm 0.023 \pm 0.002$
5.915	$0.135 \pm 0.042 \pm 0.000$	$0.073 \pm 0.022 \pm 0.002$
5.925	$0.078 \pm 0.036 \pm 0.001$	$0.079 \pm 0.023 \pm 0.002$
5.935	$0.053 \pm 0.032 \pm 0.000$	$0.065 \pm 0.020 \pm 0.002$
5.945	$0.106 \pm 0.037 \pm 0.000$	$0.030 \pm 0.016 \pm 0.001$
5.955	$0.059 \pm 0.030 \pm 0.000$	$0.056 \pm 0.023 \pm 0.001$
5.965	$0.046 \pm 0.028 \pm 0.000$	$0.107 \pm 0.025 \pm 0.003$
5.975	$0.060 \pm 0.032 \pm 0.000$	$0.056 \pm 0.019 \pm 0.002$
5.985	$0.070 \pm 0.033 \pm 0.000$	$0.042 \pm 0.017 \pm 0.001$
5.995	$0.098 \pm 0.032 \pm 0.000$	$0.038 \pm 0.015 \pm 0.001$

(Table continued)

TABLE III. The values of the $e^+e^- \to D^{*+}D^{*-}$ cross sections components and their statistical and uncorrelated systematic errors. Correlated systematic error is equal to 6%. The first tabulated error is statistical and the second is systematic.

$\sqrt{s}$ (GeV)	σ_{TT} (nb)	σ_{TL} (nb)	σ_{LL} (nb)
4.025	$0.359 \pm 0.130 \pm 0.041$	$0.517 \pm 0.171 \pm 0.009$	$0.023 \pm 0.080 \pm 0.010$
4.035	$1.252 \pm 0.220 \pm 0.131$	$1.293 \pm 0.262 \pm 0.030$	$0.170 \pm 0.129 \pm 0.031$
4.045	$1.023 \pm 0.211 \pm 0.119$	$1.37 \pm 0.277 \pm 0.037$	$0.384 \pm 0.160 \pm 0.051$
4.055	$0.975 \pm 0.204 \pm 0.105$	$1.536 \pm 0.285 \pm 0.016$	$0.481 \pm 0.173 \pm 0.049$
4.065	$1.199 \pm 0.227 \pm 0.126$	$1.103 \pm 0.273 \pm 0.033$	$0.522 \pm 0.153 \pm 0.046$
4.075	$1.163 \pm 0.221 \pm 0.128$	$1.812 \pm 0.300 \pm 0.025$	$0.413 \pm 0.176 \pm 0.055$
4.085	$1.077 \pm 0.213 \pm 0.121$	$1.627 \pm 0.295 \pm 0.032$	$0.525 \pm 0.184 \pm 0.063$
4.095	$0.831 \pm 0.173 \pm 0.093$	$1.452 \pm 0.269 \pm 0.021$	$0.473 \pm 0.175 \pm 0.059$
4.105	$0.702 \pm 0.163 \pm 0.080$	$1.498 \pm 0.241 \pm 0.001$	$0.392 \pm 0.140 \pm 0.039$
4.115	$0.808 \pm 0.185 \pm 0.099$	$1.335 \pm 0.282 \pm 0.030$	$0.930 \pm 0.193 \pm 0.079$
4.125	$0.616 \pm 0.173 \pm 0.089$	$1.791 \pm 0.289 \pm 0.022$	$0.753 \pm 0.192 \pm 0.076$
4.135	$0.908 \pm 0.180 \pm 0.101$	$0.930 \pm 0.250 \pm 0.039$	$1.157 \pm 0.198 \pm 0.089$
4.145	$1.096 \pm 0.190 \pm 0.115$	$0.888 \pm 0.246 \pm 0.041$	$0.902 \pm 0.180 \pm 0.074$
4.155	$0.892 \pm 0.207 \pm 0.119$	$1.305 \pm 0.303 \pm 0.052$	$0.918 \pm 0.198 \pm 0.083$
4.165	$0.830 \pm 0.190 \pm 0.109$	$1.461 \pm 0.272 \pm 0.031$	$0.766 \pm 0.171 \pm 0.068$
4.175	$0.987 \pm 0.187 \pm 0.111$	$0.908 \pm 0.260 \pm 0.049$	$0.940 \pm 0.193 \pm 0.083$
4.185	$0.750 \pm 0.163 \pm 0.080$	$1.309 \pm 0.256 \pm 0.008$	$0.599 \pm 0.169 \pm 0.055$
4.195	$0.874 \pm 0.171 \pm 0.089$	$0.974 \pm 0.228 \pm 0.015$	$0.524 \pm 0.147 \pm 0.045$
4.205	$0.966 \pm 0.165 \pm 0.092$	$0.530 \pm 0.199 \pm 0.030$	$0.587 \pm 0.147 \pm 0.050$
4.215	$0.369 \pm 0.120 \pm 0.045$	$0.852 \pm 0.193 \pm 0.008$	$0.302 \pm 0.127 \pm 0.032$
4.225	$0.298 \pm 0.132 \pm 0.045$	$0.496 \pm 0.197 \pm 0.022$	$0.357 \pm 0.123 \pm 0.033$
4.235	$0.012 \pm 0.035 \pm 0.019$	$0.570 \pm 0.126 \pm 0.007$	$0.101 \pm 0.079 \pm 0.014$
4.245	$0.185 \pm 0.091 \pm 0.016$	$0.123 \pm 0.121 \pm 0.011$	$0.137 \pm 0.081 \pm 0.031$
4.255	$0.088 \pm 0.071 \pm 0.007$	$0.274 \pm 0.108 \pm 0.036$	$0.027 \pm 0.051 \pm 0.008$
4.265	$0.119 \pm 0.076 \pm 0.010$	$0.379 \pm 0.118 \pm 0.046$	$0.112 \pm 0.071 \pm 0.026$
4.275	$0.181 \pm 0.086 \pm 0.014$	$0.423 \pm 0.117 \pm 0.058$	$-0.005 \pm 0.045 \pm 0.003$
4.285	$0.249 \pm 0.099 \pm 0.022$	$0.446 \pm 0.135 \pm 0.058$	$0.060 \pm 0.064 \pm 0.016$
4.295	$0.229 \pm 0.083 \pm 0.022$	$0.195 \pm 0.094 \pm 0.026$	$0.049 \pm 0.046 \pm 0.011$
4.305	$0.260 \pm 0.106 \pm 0.022$	$0.572 \pm 0.151 \pm 0.074$	$0.128 \pm 0.080 \pm 0.029$
4.315	$0.160 \pm 0.093 \pm 0.010$	$0.632 \pm 0.13 \pm 0.085$	$-0.025 \pm 0.047 \pm 0.002$
4.325	$0.045 \pm 0.071 \pm 0.002$	$0.591 \pm 0.146 \pm 0.070$	$0.175 \pm 0.090 \pm 0.040$
4.335	$0.302 \pm 0.117 \pm 0.027$	$0.375 \pm 0.166 \pm 0.042$	$0.365 \pm 0.115 \pm 0.075$
4.345	$0.332 \pm 0.119 \pm 0.028$	$0.639 \pm 0.158 \pm 0.085$	$0.072 \pm 0.066 \pm 0.019$
4.355	$0.221 \pm 0.110 \pm 0.017$	$0.810 \pm 0.176 \pm 0.101$	$0.070 \pm 0.085 \pm 0.025$
4.365	$0.181 \pm 0.100 \pm 0.013$	$0.750 \pm 0.164 \pm 0.096$	$0.092 \pm 0.078 \pm 0.025$
4.375	$0.298 \pm 0.112 \pm 0.025$	$0.790 \pm 0.143 \pm 0.103$	$0.009 \pm 0.028 \pm 0.012$
4.385	$0.199 \pm 0.097 \pm 0.016$	$0.577 \pm 0.148 \pm 0.072$	$0.126 \pm 0.080 \pm 0.031$
4.395	$0.164 \pm 0.088 \pm 0.013$	$0.769 \pm 0.154 \pm 0.096$	$0.086 \pm 0.080 \pm 0.025$
4.405	$0.400 \pm 0.107 \pm 0.039$	$0.404 \pm 0.138 \pm 0.048$	$0.110 \pm 0.083 \pm 0.029$
4.415	$0.231 \pm 0.103 \pm 0.019$	$0.740 \pm 0.168 \pm 0.090$	$0.130 \pm 0.094 \pm 0.036$
4.425	$0.146 \pm 0.075 \pm 0.013$	$0.519 \pm 0.133 \pm 0.061$	$0.084 \pm 0.079 \pm 0.025$
4.435	$0.179 \pm 0.087 \pm 0.015$	$0.494 \pm 0.135 \pm 0.062$	$0.118 \pm 0.076 \pm 0.028$
4.445	$0.107 \pm 0.076 \pm 0.010$	$0.471 \pm 0.147 \pm 0.044$	$0.080 \pm 0.096 \pm 0.034$
4.455	$0.189 \pm 0.068 \pm 0.019$	$0.159 \pm 0.090 \pm 0.016$	$0.179 \pm 0.075 \pm 0.036$
4.465	$0.210 \pm 0.088 \pm 0.021$	$0.326 \pm 0.136 \pm 0.035$	$0.091 \pm 0.084 \pm 0.027$
4.475	$0.107 \pm 0.061 \pm 0.009$	$0.221 \pm 0.087 \pm 0.029$	$0.041 \pm 0.040 \pm 0.010$
4.485	$0.114 \pm 0.069 \pm 0.009$	$0.258 \pm 0.091 \pm 0.036$	$0.024 \pm 0.040 \pm 0.006$
4.495	$0.153 \pm 0.071 \pm 0.014$	$0.354 \pm 0.105 \pm 0.044$	$0.072 \pm 0.060 \pm 0.018$
4.505	$0.136 \pm 0.087 \pm 0.011$	$0.310 \pm 0.131 \pm 0.038$	$0.076 \pm 0.071 \pm 0.020$
4.515	$-0.005 \pm 0.051 \pm 0.006$	$0.468 \pm 0.107 \pm 0.061$	$0.070 \pm 0.061 \pm 0.018$
4.525	$0.241 \pm 0.087 \pm 0.023$	$0.192 \pm 0.106 \pm 0.025$	$0.042 \pm 0.055 \pm 0.011$
4.535	$0.121 \pm 0.072 \pm 0.010$	$0.328 \pm 0.101 \pm 0.044$	$-0.004 \pm 0.035 \pm 0.002$
4.545	$0.014 \pm 0.031 \pm 0.001$	$0.453 \pm 0.118 \pm 0.048$	$0.086 \pm 0.082 \pm 0.027$
4.555	$0.067 \pm 0.052 \pm 0.005$	$0.271 \pm 0.062 \pm 0.036$	$-0.034 \pm 0.020 \pm 0.004$
4.565	$0.089 \pm 0.071 \pm 0.007$	$0.425 \pm 0.128 \pm 0.049$	$0.038 \pm 0.071 \pm 0.016$

(Table continued)

TABLE III. *(Continued)*

$\sqrt{s}$ (GeV)	σ_{TT} (nb)	σ_{TL} (nb)	σ_{LL} (nb)
4.575	$0.119 \pm 0.071 \pm 0.010$	$0.447 \pm 0.111 \pm 0.058$	$0.028 \pm 0.051 \pm 0.010$
4.585	$0.056 \pm 0.051 \pm 0.004$	$0.260 \pm 0.086 \pm 0.033$	$0.067 \pm 0.049 \pm 0.014$
4.595	$0.173 \pm 0.080 \pm 0.014$	$0.300 \pm 0.103 \pm 0.036$	$0.002 \pm 0.037 \pm 0.002$
4.605	$0.113 \pm 0.059 \pm 0.010$	$0.115 \pm 0.077 \pm 0.012$	$0.125 \pm 0.061 \pm 0.020$
4.615	$0.087 \pm 0.066 \pm 0.006$	$0.333 \pm 0.093 \pm 0.040$	$-0.009 \pm 0.031 \pm 0.000$
4.625	$0.078 \pm 0.056 \pm 0.006$	$0.239 \pm 0.090 \pm 0.026$	$0.142 \pm 0.066 \pm 0.024$
4.635	$0.058 \pm 0.068 \pm 0.002$	$0.323 \pm 0.123 \pm 0.036$	$0.105 \pm 0.076 \pm 0.020$
4.645	$0.058 \pm 0.080 \pm 0.002$	$0.379 \pm 0.132 \pm 0.043$	$0.031 \pm 0.066 \pm 0.009$
4.655	$0.080 \pm 0.060 \pm 0.006$	$0.435 \pm 0.078 \pm 0.050$	$-0.051 \pm 0.024 \pm 0.005$
4.665	$0.141 \pm 0.074 \pm 0.012$	$0.337 \pm 0.093 \pm 0.031$	$0.000 \pm 0.009 \pm 0.009$
4.675	$0.081 \pm 0.056 \pm 0.007$	$0.315 \pm 0.096 \pm 0.034$	$0.082 \pm 0.060 \pm 0.015$
4.685	$0.154 \pm 0.071 \pm 0.013$	$0.104 \pm 0.087 \pm 0.012$	$0.084 \pm 0.055 \pm 0.015$
4.695	$-0.018 \pm 0.062 \pm 0.004$	$0.738 \pm 0.140 \pm 0.078$	$-0.162 \pm 0.080 \pm 0.011$
4.705	$0.189 \pm 0.076 \pm 0.016$	$0.187 \pm 0.093 \pm 0.021$	$0.050 \pm 0.054 \pm 0.010$
4.715	$0.102 \pm 0.065 \pm 0.008$	$0.304 \pm 0.106 \pm 0.034$	$0.062 \pm 0.057 \pm 0.012$
4.725	$0.153 \pm 0.070 \pm 0.013$	$0.215 \pm 0.096 \pm 0.022$	$0.113 \pm 0.068 \pm 0.021$
4.735	$-0.057 \pm 0.025 \pm 0.006$	$0.513 \pm 0.089 \pm 0.051$	$0.094 \pm 0.075 \pm 0.022$
4.745	$0.024 \pm 0.057 \pm 0.000$	$0.421 \pm 0.118 \pm 0.046$	$0.075 \pm 0.069 \pm 0.015$
4.755	$0.101 \pm 0.064 \pm 0.008$	$0.139 \pm 0.088 \pm 0.016$	$0.047 \pm 0.049 \pm 0.009$
4.765	$0.028 \pm 0.030 \pm 0.002$	$0.235 \pm 0.080 \pm 0.024$	$0.052 \pm 0.055 \pm 0.011$
4.775	$-0.066 \pm 0.033 \pm 0.007$	$0.332 \pm 0.067 \pm 0.038$	$0.010 \pm 0.039 \pm 0.004$
4.785	$-0.171 \pm 0.084 \pm 0.024$	$0.585 \pm 0.134 \pm 0.070$	$-0.021 \pm 0.046 \pm 0.000$
4.795	$0.213 \pm 0.072 \pm 0.002$	$0.080 \pm 0.076 \pm 0.005$	$0.158 \pm 0.069 \pm 0.011$
4.805	$0.023 \pm 0.044 \pm 0.001$	$0.335 \pm 0.095 \pm 0.037$	$0.035 \pm 0.052 \pm 0.008$
4.815	$-0.006 \pm 0.024 \pm 0.001$	$0.333 \pm 0.084 \pm 0.035$	$0.024 \pm 0.052 \pm 0.008$
4.825	$0.053 \pm 0.054 \pm 0.018$	$0.163 \pm 0.077 \pm 0.008$	$0.040 \pm 0.051 \pm 0.022$
4.835	$0.161 \pm 0.064 \pm 0.015$	$0.106 \pm 0.074 \pm 0.012$	$0.076 \pm 0.049 \pm 0.012$
4.845	$0.123 \pm 0.065 \pm 0.010$	$0.100 \pm 0.081 \pm 0.012$	$0.134 \pm 0.060 \pm 0.021$
4.855	$0.064 \pm 0.045 \pm 0.005$	$0.139 \pm 0.067 \pm 0.014$	$0.085 \pm 0.053 \pm 0.015$
4.865	$0.084 \pm 0.055 \pm 0.001$	$0.105 \pm 0.074 \pm 0.013$	$0.048 \pm 0.054 \pm 0.003$
4.875	$0.023 \pm 0.037 \pm 0.002$	$0.275 \pm 0.079 \pm 0.028$	$-0.016 \pm 0.045 \pm 0.003$
4.885	$0.064 \pm 0.045 \pm 0.004$	$0.077 \pm 0.038 \pm 0.010$	$-0.011 \pm 0.006 \pm 0.003$
4.895	$0.082 \pm 0.055 \pm 0.006$	$0.167 \pm 0.076 \pm 0.020$	$0.097 \pm 0.050 \pm 0.016$
4.905	$0.000 \pm 0.029 \pm 0.001$	$0.329 \pm 0.056 \pm 0.037$	$-0.039 \pm 0.017 \pm 0.004$
4.915	$0.068 \pm 0.047 \pm 0.006$	$0.185 \pm 0.073 \pm 0.021$	$0.011 \pm 0.035 \pm 0.003$
4.925	$0.107 \pm 0.055 \pm 0.019$	$0.122 \pm 0.071 \pm 0.008$	$0.106 \pm 0.052 \pm 0.002$
4.935	$-0.018 \pm 0.037 \pm 0.027$	$0.386 \pm 0.079 \pm 0.009$	$-0.001 \pm 0.032 \pm 0.009$
4.945	$0.103 \pm 0.057 \pm 0.008$	$0.149 \pm 0.078 \pm 0.017$	$0.057 \pm 0.048 \pm 0.011$
4.955	$-0.025 \pm 0.011 \pm 0.044$	$0.409 \pm 0.013 \pm 0.015$	$0.029 \pm 0.013 \pm 0.000$
4.965	$0.026 \pm 0.033 \pm 0.002$	$0.097 \pm 0.069 \pm 0.008$	$0.147 \pm 0.062 \pm 0.024$
4.975	$0.010 \pm 0.028 \pm 0.001$	$0.142 \pm 0.066 \pm 0.014$	$0.077 \pm 0.051 \pm 0.014$
4.985	$0.091 \pm 0.047 \pm 0.004$	$0.125 \pm 0.079 \pm 0.002$	$0.030 \pm 0.036 \pm 0.003$
4.995	$0.032 \pm 0.046 \pm 0.001$	$0.154 \pm 0.065 \pm 0.019$	$0.002 \pm 0.021 \pm 0.000$
5.005	$0.047 \pm 0.044 \pm 0.003$	$0.172 \pm 0.049 \pm 0.021$	$-0.021 \pm 0.015 \pm 0.003$
5.015	$-0.017 \pm 0.017 \pm 0.004$	$0.155 \pm 0.044 \pm 0.020$	$0.022 \pm 0.028 \pm 0.004$
5.025	$-0.030 \pm 0.039 \pm 0.026$	$0.330 \pm 0.059 \pm 0.020$	$-0.028 \pm 0.019 \pm 0.007$
5.035	$0.043 \pm 0.043 \pm 0.004$	$0.156 \pm 0.082 \pm 0.014$	$0.044 \pm 0.056 \pm 0.011$
5.045	$0.023 \pm 0.042 \pm 0.001$	$0.209 \pm 0.079 \pm 0.023$	$0.036 \pm 0.045 \pm 0.008$
5.055	$-0.011 \pm 0.025 \pm 0.006$	$0.251 \pm 0.070 \pm 0.032$	$-0.017 \pm 0.046 \pm 0.015$
5.065	$-0.01 \pm 0.027 \pm 0.003$	$0.227 \pm 0.044 \pm 0.027$	$-0.027 \pm 0.014 \pm 0.003$
5.075	$0.039 \pm 0.033 \pm 0.003$	$0.164 \pm 0.067 \pm 0.017$	$0.094 \pm 0.052 \pm 0.016$
5.085	$-0.021 \pm 0.016 \pm 0.009$	$0.196 \pm 0.048 \pm 0.015$	$-0.010 \pm 0.035 \pm 0.003$
5.095	$0.058 \pm 0.041 \pm 0.004$	$0.199 \pm 0.050 \pm 0.024$	$-0.024 \pm 0.011 \pm 0.003$
5.105	$0.056 \pm 0.044 \pm 0.006$	$0.307 \pm 0.048 \pm 0.025$	$-0.057 \pm 0.017 \pm 0.011$
5.115	$0.073 \pm 0.039 \pm 0.013$	$0.086 \pm 0.053 \pm 0.013$	$0.104 \pm 0.044 \pm 0.014$
5.125	$0.087 \pm 0.031 \pm 0.012$	$0.296 \pm 0.053 \pm 0.005$	$-0.014 \pm 0.021 \pm 0.005$

(Table continued)

TABLE III. *(Continued)*

$\sqrt{s}$ (GeV)	σ_{TT} (nb)	σ_{TL} (nb)	σ_{LL} (nb)
5.135	$0.100 \pm 0.044 \pm 0.010$	$0.034 \pm 0.051 \pm 0.002$	$0.036 \pm 0.036 \pm 0.008$
5.145	$0.058 \pm 0.036 \pm 0.001$	$0.16 \pm 0.048 \pm 0.010$	$-0.016 \pm 0.016 \pm 0.005$
5.155	$0.012 \pm 0.008 \pm 0.000$	$-0.008 \pm 0.003 \pm 0.001$	$0.119 \pm 0.033 \pm 0.018$
5.165	$-0.003 \pm 0.002 \pm 0.000$	$0.117 \pm 0.041 \pm 0.011$	$0.020 \pm 0.034 \pm 0.006$
5.175	$0.000 \pm 0.020 \pm 0.001$	$0.195 \pm 0.060 \pm 0.019$	$-0.009 \pm 0.037 \pm 0.001$
5.185	$0.047 \pm 0.023 \pm 0.013$	$0.182 \pm 0.053 \pm 0.002$	$0.027 \pm 0.040 \pm 0.002$
5.195	$-0.004 \pm 0.030 \pm 0.018$	$0.154 \pm 0.033 \pm 0.015$	$-0.044 \pm 0.016 \pm 0.007$
5.205	$0.038 \pm 0.033 \pm 0.014$	$0.073 \pm 0.054 \pm 0.012$	$0.007 \pm 0.025 \pm 0.001$
5.215	$-0.042 \pm 0.005 \pm 0.005$	$0.120 \pm 0.015 \pm 0.013$	$0.020 \pm 0.027 \pm 0.004$
5.225	$-0.006 \pm 0.027 \pm 0.012$	$0.175 \pm 0.047 \pm 0.007$	$0.032 \pm 0.025 \pm 0.001$
5.235	$0.046 \pm 0.037 \pm 0.002$	$0.183 \pm 0.039 \pm 0.018$	$-0.148 \pm 0.045 \pm 0.027$
5.245	$-0.022 \pm 0.030 \pm 0.007$	$0.154 \pm 0.063 \pm 0.005$	$0.007 \pm 0.031 \pm 0.005$
5.255	$0.069 \pm 0.031 \pm 0.007$	$0.130 \pm 0.036 \pm 0.014$	$0.032 \pm 0.029 \pm 0.000$
5.265	$0.051 \pm 0.030 \pm 0.005$	$0.008 \pm 0.037 \pm 0.000$	$0.054 \pm 0.033 \pm 0.009$
5.275	$0.008 \pm 0.043 \pm 0.003$	$0.143 \pm 0.065 \pm 0.017$	$0.004 \pm 0.028 \pm 0.002$
5.285	$-0.052 \pm 0.037 \pm 0.009$	$0.244 \pm 0.044 \pm 0.030$	$-0.028 \pm 0.011 \pm 0.003$
5.295	$0.021 \pm 0.029 \pm 0.002$	$0.154 \pm 0.055 \pm 0.015$	$-0.004 \pm 0.033 \pm 0.003$
5.305	$0.004 \pm 0.026 \pm 0.008$	$0.175 \pm 0.060 \pm 0.006$	$-0.152 \pm 0.114 \pm 0.017$
5.315	$0.066 \pm 0.035 \pm 0.006$	$0.061 \pm 0.049 \pm 0.005$	$0.021 \pm 0.035 \pm 0.005$
5.325	$0.031 \pm 0.049 \pm 0.002$	$0.116 \pm 0.078 \pm 0.013$	$0.010 \pm 0.038 \pm 0.003$
5.335	$0.104 \pm 0.043 \pm 0.004$	$0.085 \pm 0.039 \pm 0.005$	$-0.011 \pm 0.013 \pm 0.001$
5.345	$0.038 \pm 0.019 \pm 0.004$	$0.185 \pm 0.045 \pm 0.024$	$0.022 \pm 0.032 \pm 0.001$
5.355	$-0.010 \pm 0.019 \pm 0.003$	$0.062 \pm 0.041 \pm 0.003$	$-0.016 \pm 0.019 \pm 0.006$
5.365	$0.039 \pm 0.035 \pm 0.014$	$0.087 \pm 0.058 \pm 0.006$	$0.129 \pm 0.052 \pm 0.009$
5.375	$-0.006 \pm 0.021 \pm 0.002$	$0.100 \pm 0.047 \pm 0.010$	$0.087 \pm 0.042 \pm 0.015$
5.385	$-0.028 \pm 0.014 \pm 0.006$	$0.246 \pm 0.044 \pm 0.024$	$-0.041 \pm 0.031 \pm 0.006$
5.395	$-0.045 \pm 0.017 \pm 0.004$	$0.133 \pm 0.029 \pm 0.013$	$0.006 \pm 0.030 \pm 0.004$
5.405	$0.019 \pm 0.027 \pm 0.004$	$0.162 \pm 0.048 \pm 0.004$	$-0.017 \pm 0.017 \pm 0.003$
5.415	$0.018 \pm 0.025 \pm 0.002$	$0.071 \pm 0.051 \pm 0.004$	$0.074 \pm 0.042 \pm 0.014$
5.425	$0.069 \pm 0.037 \pm 0.018$	$0.143 \pm 0.059 \pm 0.005$	$0.045 \pm 0.037 \pm 0.005$
5.435	$-0.015 \pm 0.014 \pm 0.003$	$0.145 \pm 0.035 \pm 0.017$	$-0.014 \pm 0.016 \pm 0.000$
5.445	$0.014 \pm 0.017 \pm 0.001$	$0.087 \pm 0.042 \pm 0.007$	$0.045 \pm 0.031 \pm 0.006$
5.455	$0.000 \pm 0.017 \pm 0.001$	$0.169 \pm 0.035 \pm 0.019$	$-0.020 \pm 0.013 \pm 0.002$
5.465	$-0.014 \pm 0.011 \pm 0.002$	$0.057 \pm 0.017 \pm 0.003$	$-0.067 \pm 0.019 \pm 0.003$
5.475	$0.071 \pm 0.032 \pm 0.013$	$0.100 \pm 0.042 \pm 0.006$	$0.028 \pm 0.029 \pm 0.010$
5.485	$0.005 \pm 0.021 \pm 0.007$	$0.178 \pm 0.041 \pm 0.006$	$-0.02 \pm 0.015 \pm 0.002$
5.495	$0.028 \pm 0.027 \pm 0.005$	$0.125 \pm 0.049 \pm 0.004$	$0.023 \pm 0.029 \pm 0.001$
5.505	$0.044 \pm 0.029 \pm 0.003$	$0.064 \pm 0.047 \pm 0.003$	$0.019 \pm 0.020 \pm 0.001$
5.515	$0.017 \pm 0.024 \pm 0.010$	$0.114 \pm 0.042 \pm 0.009$	$-0.006 \pm 0.024 \pm 0.012$
5.525	$0.015 \pm 0.024 \pm 0.000$	$0.171 \pm 0.033 \pm 0.021$	$-0.020 \pm 0.009 \pm 0.002$
5.535	$0.011 \pm 0.008 \pm 0.000$	$0.123 \pm 0.008 \pm 0.013$	$0.005 \pm 0.008 \pm 0.003$
5.545	$-0.002 \pm 0.005 \pm 0.001$	$0.073 \pm 0.029 \pm 0.005$	$0.003 \pm 0.014 \pm 0.001$
5.555	$0.023 \pm 0.015 \pm 0.007$	$0.072 \pm 0.022 \pm 0.011$	$0.003 \pm 0.007 \pm 0.004$
5.565	$0.003 \pm 0.015 \pm 0.000$	$0.053 \pm 0.031 \pm 0.005$	$0.007 \pm 0.022 \pm 0.003$
5.575	$0.003 \pm 0.010 \pm 0.000$	$0.078 \pm 0.036 \pm 0.008$	$0.022 \pm 0.026 \pm 0.004$
5.585	$0.006 \pm 0.029 \pm 0.018$	$0.150 \pm 0.119 \pm 0.010$	$0.005 \pm 0.014 \pm 0.002$
5.595	$0.047 \pm 0.028 \pm 0.004$	$0.095 \pm 0.041 \pm 0.001$	$0.020 \pm 0.023 \pm 0.000$
5.605	$0.015 \pm 0.018 \pm 0.000$	$0.043 \pm 0.015 \pm 0.006$	$-0.014 \pm 0.006 \pm 0.002$
5.615	$0.031 \pm 0.018 \pm 0.002$	$0.042 \pm 0.035 \pm 0.004$	$0.032 \pm 0.014 \pm 0.003$
5.625	$-0.010 \pm 0.015 \pm 0.002$	$0.027 \pm 0.021 \pm 0.013$	$0.06 \pm 0.027 \pm 0.008$
5.635	$0.053 \pm 0.040 \pm 0.004$	$0.056 \pm 0.062 \pm 0.006$	$0.017 \pm 0.032 \pm 0.004$
5.645	$0.011 \pm 0.014 \pm 0.002$	$0.073 \pm 0.028 \pm 0.000$	$0.006 \pm 0.011 \pm 0.000$
5.655	$0.033 \pm 0.024 \pm 0.000$	$0.039 \pm 0.036 \pm 0.013$	$0.014 \pm 0.015 \pm 0.001$
5.665	$-0.012 \pm 0.027 \pm 0.008$	$0.091 \pm 0.024 \pm 0.029$	$0.028 \pm 0.018 \pm 0.006$
5.675	$-0.047 \pm 0.012 \pm 0.006$	$0.111 \pm 0.015 \pm 0.013$	$-0.012 \pm 0.006 \pm 0.001$
5.685	$0.019 \pm 0.019 \pm 0.003$	$0.083 \pm 0.031 \pm 0.004$	$-0.004 \pm 0.014 \pm 0.001$

(Table continued)

TABLE III. *(Continued)*

$\sqrt{s}$ (GeV)	σ_{TT} (nb)	σ_{TL} (nb)	σ_{LL} (nb)
5.695	$0.030 \pm 0.019 \pm 0.003$	$0.045 \pm 0.026 \pm 0.005$	$0.003 \pm 0.014 \pm 0.001$
5.705	$0.016 \pm 0.016 \pm 0.001$	$0.085 \pm 0.032 \pm 0.009$	$0.018 \pm 0.019 \pm 0.004$
5.715	$0.037 \pm 0.026 \pm 0.001$	$0.052 \pm 0.039 \pm 0.000$	$0.012 \pm 0.025 \pm 0.002$
5.725	$0.007 \pm 0.005 \pm 0.004$	$0.079 \pm 0.007 \pm 0.004$	$0.012 \pm 0.006 \pm 0.000$
5.735	$0.028 \pm 0.044 \pm 0.006$	$0.058 \pm 0.06 \pm 0.013$	$0.033 \pm 0.049 \pm 0.005$
5.745	$0.028 \pm 0.027 \pm 0.002$	$0.024 \pm 0.031 \pm 0.004$	$0.015 \pm 0.016 \pm 0.003$
5.755	$-0.005 \pm 0.019 \pm 0.002$	$0.098 \pm 0.033 \pm 0.012$	$0.007 \pm 0.017 \pm 0.002$
5.765	$-0.006 \pm 0.012 \pm 0.004$	$-0.001 \pm 0.01 \pm 0.005$	$0.062 \pm 0.023 \pm 0.008$
5.775	$0.017 \pm 0.014 \pm 0.001$	$0.057 \pm 0.012 \pm 0.006$	$-0.020 \pm 0.005 \pm 0.002$
5.785	$-0.015 \pm 0.005 \pm 0.002$	$0.069 \pm 0.024 \pm 0.008$	$0.021 \pm 0.020 \pm 0.004$
5.795	$0.048 \pm 0.025 \pm 0.000$	$0.041 \pm 0.026 \pm 0.000$	$0.001 \pm 0.011 \pm 0.002$
5.805	$-0.005 \pm 0.012 \pm 0.002$	$0.101 \pm 0.032 \pm 0.005$	$-0.015 \pm 0.013 \pm 0.003$
5.815	$-0.009 \pm 0.013 \pm 0.008$	$0.110 \pm 0.03 \pm 0.007$	$-0.019 \pm 0.021 \pm 0.005$
5.825	$0.052 \pm 0.026 \pm 0.004$	$0.019 \pm 0.024 \pm 0.003$	$0.010 \pm 0.012 \pm 0.002$
5.835	$0.039 \pm 0.015 \pm 0.007$	$0.037 \pm 0.019 \pm 0.005$	$0.060 \pm 0.020 \pm 0.005$
5.845	$-0.016 \pm 0.013 \pm 0.005$	$0.061 \pm 0.027 \pm 0.001$	$-0.013 \pm 0.020 \pm 0.004$
5.855	$-0.012 \pm 0.004 \pm 0.001$	$0.115 \pm 0.03 \pm 0.013$	$0.002 \pm 0.023 \pm 0.002$
5.865	$-0.04 \pm 0.009 \pm 0.004$	$0.107 \pm 0.014 \pm 0.012$	$-0.051 \pm 0.020 \pm 0.006$
5.875	$-0.011 \pm 0.009 \pm 0.003$	$0.106 \pm 0.012 \pm 0.014$	$-0.085 \pm 0.011 \pm 0.011$
5.885	$0.042 \pm 0.022 \pm 0.004$	$0.015 \pm 0.026 \pm 0.001$	$0.038 \pm 0.021 \pm 0.006$
5.895	$-0.008 \pm 0.010 \pm 0.002$	$0.054 \pm 0.024 \pm 0.006$	$0.023 \pm 0.018 \pm 0.004$
5.905	$0.002 \pm 0.011 \pm 0.002$	$0.050 \pm 0.028 \pm 0.009$	$0.002 \pm 0.009 \pm 0.001$
5.915	$0.007 \pm 0.012 \pm 0.004$	$0.069 \pm 0.023 \pm 0.004$	$-0.007 \pm 0.008 \pm 0.000$
5.925	$0.010 \pm 0.024 \pm 0.002$	$0.030 \pm 0.033 \pm 0.002$	$0.009 \pm 0.013 \pm 0.000$
5.935	$0.007 \pm 0.014 \pm 0.000$	$0.049 \pm 0.011 \pm 0.006$	$-0.006 \pm 0.001 \pm 0.001$
5.945	$-0.014 \pm 0.022 \pm 0.003$	$0.056 \pm 0.014 \pm 0.007$	$-0.007 \pm 0.002 \pm 0.001$
5.955	$0.034 \pm 0.011 \pm 0.003$	$0.069 \pm 0.021 \pm 0.009$	$0.032 \pm 0.022 \pm 0.001$
5.965	$-0.011 \pm 0.016 \pm 0.004$	$0.158 \pm 0.026 \pm 0.014$	$-0.046 \pm 0.011 \pm 0.008$
5.975	$0.033 \pm 0.011 \pm 0.002$	$0.079 \pm 0.019 \pm 0.008$	$-0.006 \pm 0.003 \pm 0.002$
5.985	$0.019 \pm 0.013 \pm 0.005$	$0.041 \pm 0.022 \pm 0.004$	$0.029 \pm 0.022 \pm 0.003$
5.995	$0.052 \pm 0.012 \pm 0.001$	$0.009 \pm 0.019 \pm 0.002$	$0.013 \pm 0.009 \pm 0.000$

[1] C. Patrignani *et al.* (Particle Data Group), Chin. Phys. C **40**, 100001 (2016).
[2] M. Ablikim *et al.* (BES Collaboration), Phys. Lett. B **660**, 315 (2008).
[3] B. Aubert *et al.* (*BABAR* Collaboration), Phys. Rev. Lett. **95**, 142001 (2005).
[4] B. Aubert *et al.* (*BABAR* Collaboration), arXiv:0808.1543.
[5] B. Aubert *et al.* (*BABAR* Collaboration), Phys. Rev. Lett. **98**, 212001 (2007).
[6] K. Abe *et al.* (Belle Collaboration), arXiv:hep-ex/0612006.
[7] C. Z. Yuan *et al.* (Belle Collaboration), Phys. Rev. Lett. **99**, 182004 (2007).
[8] X. L. Wang *et al.* (Belle Collaboration), Phys. Rev. Lett. **99**, 142002 (2007).
[9] X. L. Wang *et al.* (Belle Collaboration), Phys. Rev. D **91**, 112007 (2015).
[10] Z. Q. Liu *et al.* (Belle Collaboration), Phys. Rev. Lett. **110**, 252002 (2013).
[11] E. Eichten, K. Gottfried, T. Kinoshita, K. D. Lane, and T. M. Yan, Phys. Rev. D **21**, 203 (1980).
[12] G. Pakhlova *et al.* (Belle Collaboration), Phys. Rev. D **77**, 011103 (2008).
[13] G. Pakhlova *et al.* (Belle Collaboration), Phys. Rev. Lett. **98**, 092001 (2007).
[14] G. Pakhlova *et al.* (Belle Collaboration), Phys. Rev. Lett. **100**, 062001 (2008).
[15] G. Pakhlova *et al.* (Belle Collaboration), Phys. Rev. Lett. **101**, 172001 (2008).
[16] G. Pakhlova *et al.* (Belle Collaboration), Phys. Rev. D **80**, 091101 (2009).
[17] G. Pakhlova *et al.* (Belle Collaboration), Phys. Rev. D **83**, 011101 (2011).
[18] B. Aubert *et al.* (*BABAR* Collaboration), Phys. Rev. D **76**, 111105 (2007).
[19] B. Aubert *et al.* (*BABAR* Collaboration), Phys. Rev. D **79**, 092001 (2009).

[20] P. A. Sanchez *et al.* (*BABAR* Collaboration), Phys. Rev. D **82**, 052004 (2010).
[21] D. Cronin-Hennessy *et al.* (CLEO Collaboration), Phys. Rev. D **80**, 072001 (2009).
[22] A. J. Bevan *et al.* (*BABAR* and Belle Collaborations), Eur. Phys. J. C **74**, 3026 (2014).
[23] T. V. Uglov, Y. S. Kalashnikova, A. V. Nefediev, G. V. Pakhlova, and P. N. Pakhlov, JETP Lett. **105**, 1 (2017).
[24] A. Abashian *et al.* (Belle Collaboration), Nucl. Instrum. Methods Phys. Res., Sect. A **479**, 117 (2002).
[25] S. Kurokawa and E. Kikutani, Nucl. Instrum. Methods Phys. Res., Sect. A **499**, 1 (2003), and other papers included in this volume.
[26] G. Rodrigo, H. Czyz, and J. H. Kuhn, arXiv:hep-ex/0205097.
[27] K. Miyabayashi *et al.* (Belle Collaboration), Nucl. Instrum. Methods Phys. Res., Sect. A **494**, 298 (2002).
[28] E. Nakano, Nucl. Instrum. Methods Phys. Res., Sect. A **494**, 402 (2002).
[29] E. A. Kuraev and V. S. Fadin, Sov. J. Nucl. Phys. **41**, 466 (1985).
[30] J. D. Richman, California Institute of Technology Report No. CALT-68-1148, 1984.
[31] A. G. Grozin and M. Neubert, Phys. Rev. D **55**, 272 (1997).
[32] H. Georgi, in *Proceedings of the Theoretical Advanced Study Institute, 1991*, edited by R. K. Ellis, C. T. Hill, and J. D. Lykken (World Scientific, Singapore, 1992), p. 589.